Quantitative MRI maps of human neocortex explored using cell type-specific gene expression analysis

Luke J. Edwards[1,*], Peter McColgan[1,2], Saskia Helbling[1,3], Angeliki Zarkali[4], Lenka Vaculčiaková[1], Kerrin J. Pine[1], Fred Dick[5], and Nikolaus Weiskopf[1,6]

[1]Department of Neurophysics, Max Planck Institute for Human Cognitive and Brain Sciences, Leipzig, DE.

[2]Huntington's Disease Centre, University College London, UK.

[3]Poeppel Lab, Ernst Strüngmann Institute (ESI) for Neuroscience in Cooperation with Max Planck Society, Frankfurt am Main, DE.

[4]Dementia Research Centre, University College London, UK.

[5]Birkbeck/UCL Centre for Neuroimaging (BUCNI), London, UK.

[6]Felix Bloch Institute for Solid State Physics, Faculty of Physics and Earth Sciences, Leipzig University, Leipzig, DE.

*Corresponding author: Dr. Luke J. Edwards, Max Planck Institute for Human Cognitive and Brain Sciences, Stephanstraße 1A, D-04103 Leipzig, DE; tel:+49 341 9940-2428; fax:+49 341 9940-104; email:ledwards@cbs.mpg.de

Running title: QMRI explored using cell type-specific analysis

Abstract

Quantitative MRI (qMRI) allows extraction of reproducible and robust parameter maps. However, the connection to underlying biological substrates remains murky, especially in the complex, densely packed cortex. We investigated associations in human neocortex between qMRI parameters and neocortical cell types by comparing the spatial distribution of the qMRI parameters longitudinal relaxation rate (R_1), effective transverse relaxation rate ($R_2{}^*$), and magnetization transfer saturation (MTsat) to gene expression from the Allen Human Brain Atlas, then combining this with lists of genes enriched in specific cell types found in the human brain. As qMRI parameters are magnetic field strength-dependent, the analysis was performed on MRI data at 3T and 7T. All qMRI parameters significantly covaried with genes enriched in GABA- and glutamatergic neurons, i.e. they were associated with cytoarchitecture. The qMRI parameters also significantly covaried with the distribution of genes enriched in astrocytes ($R_2{}^*$ at 3T, R_1 at 7T), endothelial cells (R_1 and MTsat at 3T), microglia (R_1 and MTsat at 3T, R_1 at 7T), and oligodendrocytes (R_1 at 7T). These results advance the potential use of qMRI parameters as biomarkers for specific cell types.

Keywords: hMRI; isocortex; magnetic resonance imaging; myelin; relaxometry

Introduction

Multiparameter mapping (MPM) protocols allow rapid and efficient acquisition of relaxometric quantitative MRI (qMRI) parameters in vivo (Tabelow et al., 2019) robustly and reproducibly (Leutritz et al., 2020). These parameters include the longitudinal relaxation rate (R_1), magnetisation transfer saturation (MTsat), and effective transverse relaxation rate ($R_2{}^*$). In vivo histology aims to take such quantitative maps and extract information about the underlying microscopic biological substructures beyond the resolution of MRI (Edwards et al., 2018; Weiskopf et al., 2021).

On the whole-brain level, contrast in the above qMRI parameters is mainly driven by two main sources: macromolecules (mostly myelin), and iron (Callaghan et al., 2015; Edwards et al., 2018; Möller et al., 2019; Kirilina et al., 2020; Weiskopf et al., 2021). MTsat is interpreted as a marker for macromolecules (Georgiadis et al., 2021), $R_2{}^*$ is interpreted as a marker for mainly iron content with some sensitivity to macromolecules (Langkammer et al., 2010; Kirilina et al., 2020), and R_1 is interpreted as a marker for mainly macromolecular content with some sensitivity to iron (Callaghan et al., 2015). The sensitivity of qMRI parameters to different sources is known to vary with the static magnetic field strength (Peters et al., 2007; Rooney et al., 2007; Wang et al., 2020).

These relatively simple interpretations of qMRI parameters do not, however, allow us to infer information about the cellular architecture of the brain from their values. On the cellular level, the human neocortex is a complex, densely packed structure containing billions of neurons and glia (Lent et al., 2012). The distribution of these neurons and glia varies over the brain, forming laminae and cortical areas which can be distinguished under the microscope (Edwards et al., 2018). Herein we aim to investigate the relationship between neocortical cellular architecture and qMRI parameters by comparing spatial differences in expression of cell type-specific genes with the spatial distribution of the qMRI parameters.

Gene expression differences reflect and determine different cell types; differential gene expression throughout the neocortex can thus be related to differential expression of cell types (Lein et al., 2017; Arnatkevičiūtė et al., 2019; Fornito et al., 2019). The combination

of knowledge of cell type-specific genes (Zeisel et al., 2015; Hawrylycz et al., 2015; Hodge et al., 2019) with the cortical gene expression results found in the Allen Human Brain Atlas (AHBA) of gene expression (Hawrylycz et al., 2012) from the Allen Institute for Brain Science (AIBS) has shed light on the biological substrates of several different MRI parameters in the cortex (e.g. Whitaker et al. (2016); Shin et al. (2018); Wen et al. (2018); Liu et al. (2019); Patel et al. (2019, 2020); McColgan et al. (2021)).

Patel et al. (2020) examined the cell type-specific associations with a number of different qMRI parameters at a static magnetic field strength of 3T, including R_1 and a measure of magnetisation transfer (the magnetisation transfer ratio, MTR) in a large young male cohort. Despite the common biophysical interpretation of these two parameters as markers of macromolecular content, and thus predominantly of myelin (Edwards et al., 2018), no significant association was found to the oligodendrocyte cells (ODCs) which build myelin (Möller et al., 2019). Instead, R_1 was associated with gene expression enriched in astrocytes and CA1-pyramidal neurons, and MTR was associated with gene expression enriched in CA1-pyramidal neurons and S1-pyramidal neurons (Patel et al., 2019). This accords with our observations using an MPM protocol at 3T in a smaller healthy adult cohort using a similar method of gene expression analysis (Edwards et al., 2019). Interestingly, Patel et al. (2020) found that maps of transverse relaxation rate (R_2) and the R_2-derived myelin water fraction did show sensitivity to the ODCs. However, their analysis had several limitations, namely the use of a relatively coarse cortical atlas, cell type-specific gene expression lists based on mouse tissue rather than human tissue, and only male participants.

Genetic correlates of $R_2{}^*$ at 3T were investigated in Wen et al. (2018). The authors found that after removing some vascular-related MRI signal contributions, the spatial distribution of $R_2{}^*$ values were associated with the distribution of genes with ontologies related to neurons, glia (including astrocytes, microglia, and oligodendrocyte progenitor cells [OPCs]), and endothelial cells. At 7T, $R_2{}^*$ has also been found to be associated with cytoarchitecture, specifically with neuronal cell counts from post-mortem atlases (McColgan et al., 2021).

In order to further investigate the biophysical inferences that are possible from the quantitative parameters R_1, MTsat, and $R_2{}^*$, in the following we examine associations of the parameters using a finer cortical atlas (Glasser et al., 2016) than Patel et al. (2020), and cell type-specific gene expression lists from human tissue (Habib et al., 2017; Hodge et al., 2019). The analysis is replicated using two cell type-specific gene expression lists to reduce the possibility that the results are dependent on a specific dataset. Because qMRI parameter contrast changes with the static magnetic field strength of the MRI scanner (Rooney et al., 2007; Peters et al., 2007; Wang et al., 2020), and this could potentially give rises to changes in sensitivity and specificity (Mancini et al., 2020), we investigate the associations at two different field strengths, 3T and 7T. To mitigate partial volume effects when examining the 1.6–4.5 mm thin cortex (Edwards et al., 2018), we exclusively use high, isotropic resolution data (800 µm at 3T and 500 µm at 7T).

Materials and Methods

MRI acquisition and preprocessing

3T acquisition: We used MPM data (Weiskopf et al., 2013; Carey et al., 2018) from 17 healthy volunteers (5 female, 12 male, mean age ± standard deviation: 29.2 ± 6.8 years) from the MEG UK database (`https://meguk.ac.uk/database`), acquired on a 3T Prisma equipped with a 32-channel receive radiofrequency (RF) head coil (Siemens Healthineers, Erlangen, Germany) and a body RF receive coil at the Wellcome Centre for Human Neuroimaging, UCL, London, following the same high resolution protocol as in Bonaiuto et al. (2018). The MPM protocol consisted of three RF- and gradient-spoiled, multi-echo 3D FLASH scans with PD-, T1-, and MT-weighting (PDw, T1w, and MTw) at 800 µm isotropic resolution, plus a map of the RF transmit field B_1 acquired using a 3D-EPI spin echo/stimulated echo method (SE/STE) corrected for geometric distortions due to spatial inhomogeneities in the static magnetic field B_0 (Lutti et al., 2010). PDw: repetition time (TR) 25 ms; 8 equispaced echoes with echo time (TE) [2.34,...,18.44] ms; flip angle (FA) 6°. T1w: TR 25 ms; 8 equispaced echoes with TE [2.34,...,18.44] ms; FA

21°. MTw: TR 25 ms; 6 equispaced echoes with TE [2.34,. . . ,13.84] ms; FA 6°; Gaussian RF magnetisation transfer (MT) saturation pulse 2 kHz off resonance, 4 ms duration, nominal flip angle 220° prior to each FLASH excitation. Additional parameters: matrix size (read × phase × partition) 320 × 280 × 224, GRAPPA (Griswold et al., 2002) 2 × 2, non-selective sinc excitation, readout bandwidth 488 Hz/pixel.

7T acquisition: MPM data from 10 healthy volunteers (6 female, 4 male, 28±3.6 years) were acquired on a 7T whole-body MRI system (Magnetom 7T, Siemens Healthineers, Erlangen, Germany) equipped with a 1-channel transmit/32-channel receive RF head coil (Nova Medical, Wilmington, MA, USA) at the Max Planck Institute for Human Cognitive and Brain Sciences, Leipzig; this data was previously used in McColgan et al. (2021). The MPM protocol consisted of two RF- and gradient-spoiled, multi-echo 3D FLASH scans (PDw, T1w) adapted for whole-brain coverage at 500 µm isotropic resolution (Trampel et al., 2019), plus a map of B_1 using a 3D-EPI SE/STE method adapted for 7T corrected for geometric distortions due to inhomogeneities in B_0 (Lutti et al., 2012). PDw: TR 25 ms, 6 equispaced echoes with TE [2.8,. . . ,16] ms, FA 5°. T1w: TR 25 ms, 6 equispaced echoes with TE [2.8,. . . ,16] ms, FA 24°. Additional parameters: matrix size (read×phase× fast/inner phase encode direction) 496×434×352, GRAPPA (Griswold et al., 2002) 2×2, non-selective sinc excitation, readout bandwidth 420 Hz/pixel. To mitigate the large B_1 inhomogeneity at 7T, two dielectric pads (Webb, 2011) were placed around the head of each subject (one each side) at approximately the level of the temporal lobe. The transmit voltage was calibrated to be optimal over the occipital lobe using an initial low-resolution transmit field map. For the purposes of prospective motion correction (Zaitsev et al., 2015), each subject was scanned while wearing a tooth clip assembly (moulded to their front teeth) with an attached passive Moiré pattern marker (Vaculčiaková et al., 2022). An optical tracking system (Kineticor, Honolulu, HI, USA) tracked the motion of this marker (and thus motion of the head), allowing prospective rigid-body correction of the field of view.

The studies were approved by the local ethics committees and all subjects gave written informed consent before being scanned.

MRI data at each field strength were converted to qMRI maps of R_1, $R_2{}^*$, proton density (PD), and (at 3T only) MTsat using the hMRI toolbox (Tabelow et al., 2019, `http://hmri.info`). MTsat maps were not computed at 7T because specific absorption rate (SAR) limits at this field strength (Collins et al., 2004) hindered the acquisition of high-quality MTw images.

Cortical surfaces were reconstructed using the `recon-all` pipeline from FreeSurfer (Fischl et al., 2004, `https://surfer.nmr.mgh.harvard.edu`). Because the contrast in the 3T and 7T qMRI maps deviates significantly from the T1w MPRAGE image contrast expected by the `recon-all` pipeline (Carey et al., 2018), the following steps were taken to extract an image with MPRAGE-like contrast from the 3T and 7T qMRI parameters (McColgan et al., 2021). First, a small number of negative and very high values produced by estimation errors were set to zero in the R_1 and PD maps, such that $T_1(= 1/R_1)$ was bounded between $[0, 8000]$ ms and PD between $[0, 200]$%. Then, the PD and T_1 maps were used as input to the FreeSurfer `mri_synthesize` routine to create a synthetic FLASH volume with optimal white matter (WM)/grey matter (GM) contrast (TR 20 ms, FA 30°, TE 2.5 ms). This synthetic image was used as the input to SPM segment (`https://www.fil.ion.ucl.ac.uk/spm`) to create a combined GM/WM/cerebrospinal fluid (CSF) brain mask (threshold: tissue probability > 0), which was used for skull stripping.

For the 3T MPMs, the skull-stripped synthetic image was then used as input for the remaining steps of the `recon-all` pipeline.

At 7T, using the skull-stripped synthesized image as input to FreeSurfer frequently led to errors in the `recon-all` pipeline (McColgan et al., 2021). Thus, at 7T the PD map (normalised such that the average WM intensity is 69% (Tabelow et al., 2019)) was subtracted from 100% (i.e. the contrast was inverted) to yield an MPRAGE-like contrast. This map was then denoised (Maggioni et al., 2013, `http://www.cs.tut.fi/~foi/GCF-BM3D`) to mitigate the increased noise levels in the higher-resolution 7T data compared to 3T, and the brain mask from the synthetic image was applied. The resulting denoised and masked map was then used in the `recon-all` pipeline.

For both field strengths, cortical qMRI parameter values were mapped onto the surface using values sampled at 50% of the estimated vertex-wise cortical depth (i.e. we sampled at approximately the central cortical surface) and 2D-smoothed on the surface with a 6 mm full-width half-maximum (FWHM) kernel. Finally, FreeSurfer was used to perform surface based registration of the HCP-MMP1.0 cortical atlas (Glasser et al., 2016) from `fsaverage` template space (Mills, 2016) to subject space (CJ Neurolab, 2018).

Cell type-specific gene expression analysis

The cell type-specific gene expression analysis proceeded in two steps, described in detail below. In the first step, we constructed target gene lists from the genes with the strongest spatial associations between the AHBA gene expression data and each of the qMRI parameters using partial least squares (PLS) regression. The second step examined whether these target genes were expressed more than expected by chance within particular cell types using the Expression Weighted Cell type Enrichment (EWCE) toolbox (Skene and Grant, 2016).

The AHBA of gene expression (Hawrylycz et al., 2012) was mapped into the 180 parcellation units of the left hemisphere of the HCP-MMP1.0 atlas (Glasser et al., 2016) by following steps 1–6 in Arnatkevičiūtė et al. (2019) using code available at `https://github.com/BMHLab/AHBAprocessing` to give a (gene $\times$ region of interest (RoI)) matrix. The code was run using the options recommended by Arnatkevičiūtė et al. (2019). Only left hemisphere data are presented as right hemisphere data are not available for all AHBA donors. Three areas in the HCP-MMP1.0 atlas – retroinsular cortex, middle temporal area, and area anterior 10p (Glasser et al., 2016) – did not robustly contain samples in the AHBA and were thus omitted from further analyses. This resulted in a (gene $\times$ RoI) matrix of size $10,027 \times 177$.

Each qMRI parameter at each field strength was averaged within each parcellation unit of the left hemisphere of the HCP-MMP1.0 atlas defined in `fsaverage` space (Mills, 2016), and also over subjects, resulting in an (RoI $\times$ qMRI parameter) vector of size 177×1. Each vector was standardised by subtracting the mean and dividing by the

standard deviation over the elements in the vector before further analysis. Dimensional reduction was performed separately for each qMRI parameter using PLS regression (Rosipal and Krämer, 2006; Abdi, 2010; Krishnan et al., 2011) into the two PLS components which explained the most covariance between the spatial distribution of the genes and the spatial distribution of the qMRI parameter. The predictor variable in each case comprised the (gene $\times$ RoI) matrix, and the response variable the (RoI $\times$ qMRI parameter) vector. Weights representing the contribution of each gene to each PLS component were estimated using the bootstrapping procedure described in Vértes et al. (2016) with 10,000 bootstrapped samples. Target lists representing the top 5%, 10% and 20% of genes most positively associated (upweighted) and most negatively associated (downweighted) with each qMRI parameter were then created from these weights. We examined upweighted and downweighted associations separately to avoid potentially masking cell type associations. We only investigated components explaining $>$ 10% of the variance in the (RoI $\times$ qMRI parameter) matrix further.

To check whether our results were dependent on the cell type-specific gene sets used, we performed the further analysis steps using human-derived cell type-specific gene sets from two independent sources. Both of these datasets used RNA sequencing (RNA-seq) methods, giving sufficient dynamic range for EWCE analysis (Skene and Grant, 2016).

The first is the SMART-seq dataset (Hawrylycz et al., 2015; Hodge et al., 2019), which was downloaded from the AIBS Brain Map website (`https://portal.brain-map.org/atlases-and-data/rnaseq`; Multiple Cortical Areas - SMART-seq (2019)). These gene sets comprise gene expression sampled in cells belonging to the major cell types: astrocytes, endothelial cells, GABAergic (inhibitory) neurons, glutamatergic (excitatory) neurons, microglia, pericyte cells, vascular and leptomeningeal cells (VLMCs), oligodendrocytes (ODCs), and oligodendrocyte precursor cells (OPCs) (Hodge et al., 2019).

The second is the DroNc-seq dataset from the Regev laboratory (Habib et al., 2017). This has slightly different cell categories as it was derived from different regions (in parentheses are the abbreviations used in the dataset): astrocytes (ASC), endothelial cells (END), GABAergic neurons, glutamatergic neurons from the prefrontal cortex (exPFC),

granule neurons from the hippocampal dentate gyrus region (exDG), ODCs, OPCs, microglia (MG), pyramidal neurons from the hippocampal CA region (exCA), and neuronal stem cells (NSC).

It was shown in Hodge et al. (2019, Extended Data Fig. 5) that correspondence can be made between the labels in the two datasets, namely between the respective labels for astrocytes, microglia, endothelial cells, ODCs, OPCs and GABAergic neurons, and between the SMART-seq glutamatergic neuron and the DroNc-seq exPFC neuron labels. As the exCA, exDG, and NSC categories from the DroNc-seq dataset and the pericyte and VLMC categories from the SMART-seq dataset do not have analogues in the other respective dataset, we do not explore the results involving these cell types in the main text. Those results can be found in the Supplementary Material (Figures S1–S12).

The EWCE toolbox (`https://github.com/NathanSkene/EWCE`; version 1.2.0) was used to determine whether genes within the target lists from the PLS components of each qMRI parameter have higher expression within a particular cell type than expected by chance (Skene and Grant, 2016; Zarkali et al., 2020a,b). For a given cell type-specific dataset (here, either the SMART-seq or DroNc-seq dataset), for each cell type, c, EWCE first computes the average expression of each gene in the cell type. A sum is then made over the average expression values within the gene list associated within a target list, X, to obtain a single EWCE value for each cell type, $\gamma(X, c)$. To test the statistical significance of this value, it is compared with values obtained for bootstrap target lists, X', using the genes indexed in the cell type-specific dataset. Each comparison was run with 100,000 bootstrap lists (controlling for transcript length and GC (guanine-cytosine) content (Skene and Grant, 2016)), and statistical significance for each comparison was set at a Benjamini–Hochberg false-discovery-rate (FDR) corrected $p < 0.05$. To check robustness, the comparisons were repeated for target lists comprising the top 5%, 10% and 20% of genes associated with each parameter. Results are visualised as the number of standard deviations by which $\gamma(X, c)$ deviates from the mean over the bootstrapped samples, $\overline{\gamma(X', c)}$ (Skene and Grant, 2016).

We take an association with a cell type to be robust if there is significant overlap with

genes enriched in that cell type in both cell type-specific datasets at the top 5%-of-genes level. Note that differences in the effect size are to be expected between the two datasets as they are taken from different brain areas and used different sequencing methods. Because the signs of the PLS weights are difficult to interpret for MRI metrics (Romero-Garcia et al., 2019), we treat associations with upweighted genes and with downweighted genes identically and do not try to interpret them in terms of positive or negative correlations.

R_1 at 7T is affected by B_1 and B_0 inhomogeneities in the inferior temporal and frontal lobes (McColgan et al., 2021). These inhomogeneities become more important at 7T because their causes (B_1 field-focusing in brain-sized objects (Hoult, 2000) and (dynamic) susceptibility-induced contributions to the local B_0 field (Van de Moortele et al., 2002; Stockmann and Wald, 2018)) both increase from 3T to 7T. We thus also repeated the above analysis for R_1 at 7T after excluding data from two potentially strongly affected regions (the orbitofrontal complex and area TE2 anterior (Glasser et al., 2016), the two areas which had R_1 values which were more than three standard deviations away from the mean) to evaluate the potential influence of these artefacts.

Results

The spatial distributions of the quantitative parameters averaged over subjects at each magnetic field strength are shown in Figure 1. Primary cortical areas are clearly delineated, and subtle differences can be seen between the parameters, especially towards the posterior of the brain, around the superior temporal lobe, and (for R_1 at 7T) around the central sulcus. The differences between 3T and 7T R_1 around the inferior frontal and temporal lobes are potentially driven by artefacts arising from the greater B_1 and B_0 inhomogeneities at 7T (McColgan et al., 2021).

The spatial distribution of the PLS components in Figure 1 show a lot of similarity to the qMRI parameters, implying that we are reasonably capturing the spatial variance. The first component is very similar between all qMRI parameters, but with specific differences seen around the central sulcus in R_1 at 7T, in line with the different spatial distribution of

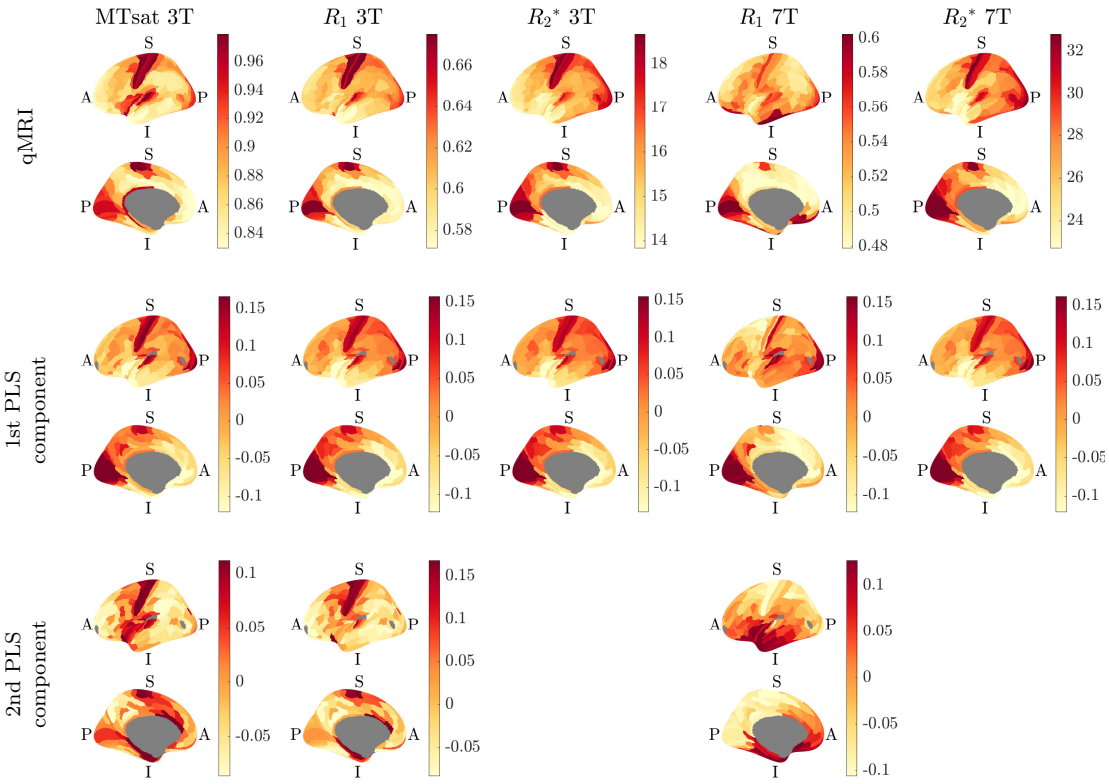

Figure 1: The left hemisphere spatial distribution of the qMRI parameters at each magnetic field strength (top row) and of the respective first and second PLS components (bottom two rows) projected on the inflated FreeSurfer `fsaverage` brain. The qMRI parameter plots show the mean over vertices and subjects in each area of the HCP-MMP1.0 atlas (units: MTsat/p.u.; R_1/s^{-1}; R_2^*/s^{-1}). The PLS component plots show the score-vectors (Rosipal and Krämer, 2006) of the (gene $\times$ RoI) matrix for each qMRI parameter, giving a visual representation of the latent PLS variables (in arbitrary units). PLS components are only plotted when they explain $> 10\%$ of the spatial variance of a qMRI parameter (Table 1). In each case, top: lateral view, bottom: medial view. A: anterior, P: posterior, I: inferior, S: superior. The regions marked in grey represent areas with no data, i.e. non-cortical tissue (mostly corpus callosum) and regions without robust cortical samples in the AHBA. Lower and upper limits of the colour maps in each plot are the 5th and 95th percentiles of the data, respectively. Colours from `http://colorbrewer.org` by Cynthia A. Brewer, Geography, Pennsylvania State University via `https://github.com/DrosteEffect/BrewerMap`.

	PLS component	Spatial variance explained in: gene distribution	qMRI parameter
R_2^* 3T	1	22%	75%
	2	7%	6%
R_2^* 7T	1	22%	71%
	2	9%	6%
MTsat 3T	1	21%	33%
	2	9%	21%
R_1 3T	1	22%	60%
	2	7%	11%
R_1 7T	1	12%	22%
	2	15%	12%

Table 1: Variance explained by the PLS components for each qMRI parameter.

the parameter in this region. The second component (plotted when the variance explained in the qMRI parameter was $> 10\%$) captures more of the differences between the spatial distributions of the qMRI parameters.

Table 1 shows that the first PLS component explained more than 50% of the spatial variance of R_1 at 3T and of R_2^* at both 3T and 7T, but less than 50% of the spatial variance of R_1 at 7T or of MTsat at 3T. For R_1 at 3T and 7T and MTsat at 3T the second PLS component explained more than 10% of the spatial variance and was therefore included in the further analysis.

The EWCE analysis results are summarised in Figure 2 and detailed for each qMRI parameter separately in Figures 3–5. The robust cell type-associations are shown in black in Figure 2. In the following we go through the results for each qMRI parameter in turn.

At 3T R_2^* showed robust associations with astrocytes, GABAergic neurons, and glutamatergic neurons (Figures 2 and 3). There was also a significant association at the top 5% level with microglia in the DroNc-seq dataset and with OPCs in the SMART-seq dataset, but these each only replicated at the top 10% level in the other dataset (Figures 2, S2, and S5).

At 7T the R_2^* results were similar to those at 3T (Figures 2 and 3). Robust associa-

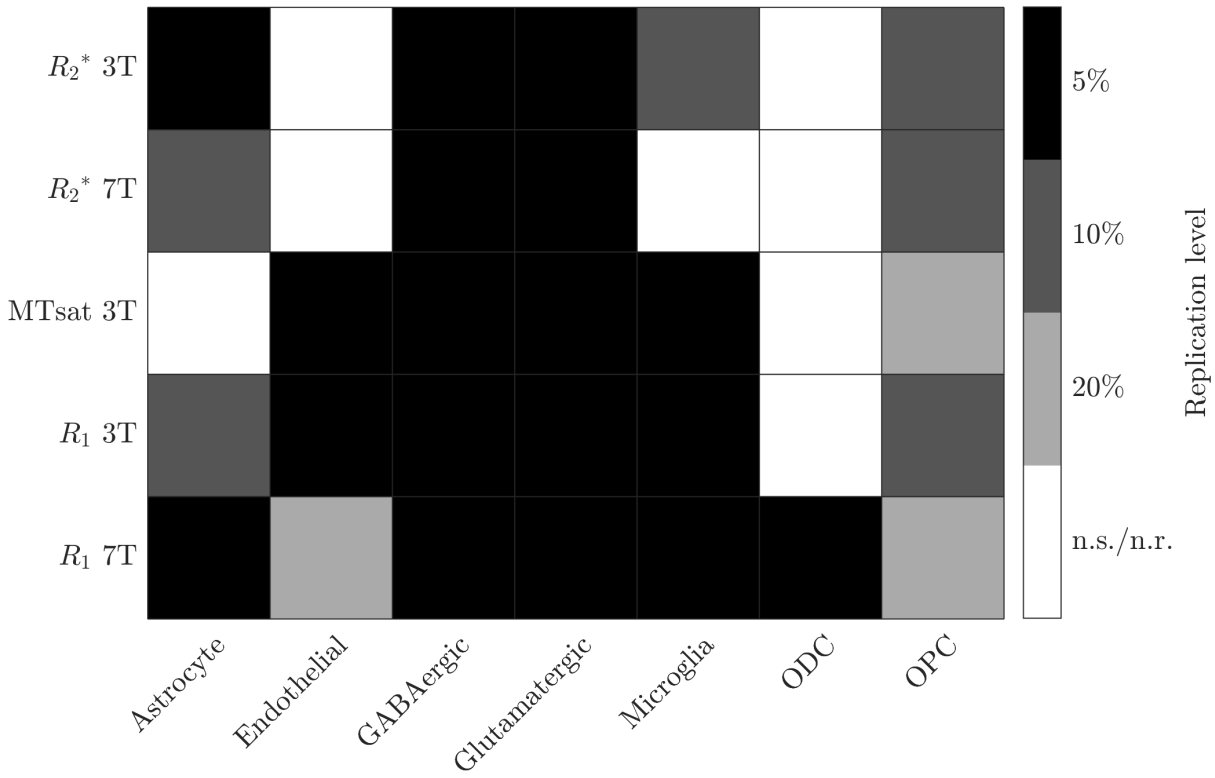

Figure 2: Summary of the significant, replicated associations found between cell type specific gene expression in the genes associated with each qMRI parameter. Replications at the level of the top 5% of genes associated with each qMRI parameter (robust associations) are shown in black, with replications at lower levels in shades of grey. Non-significant (n.s.) and non-replicating (n.r.) associations are in white.

tions were seen with GABAergic and glutamatergic neurons. Significant associations with astrocytes and OPCs were seen at the top 5% level in the SMART-seq dataset, but these only replicated at the top 10% level in the DroNc-seq dataset (Figures 2, 3, and S5).

MTsat showed robust associations with endothelial cells, GABAergic neurons, glutamatergic neurons, and microglia (Figures 2 and 4). A significant association was seen with OPCs at the top 5% level in the SMART-seq dataset for the first PLS component and in the DroNc-seq dataset for the second PLS component, but these results only replicated at the top 20% level in the respective other dataset (Figures S6, and S9).

At 3T R_1 showed robust associations with endothelial cells, GABAergic neurons, glutamatergic neurons, and microglia (Figures 2 and 5), showing some similarity to the MTsat results (Figure 4). Significant associations were also seen with astrocytes and OPCs at the top 5% level in the SMART-seq dataset for the first PLS component, but these only replicated at the top 10% (Figure S5) and top 20% (Figure S6) levels in the

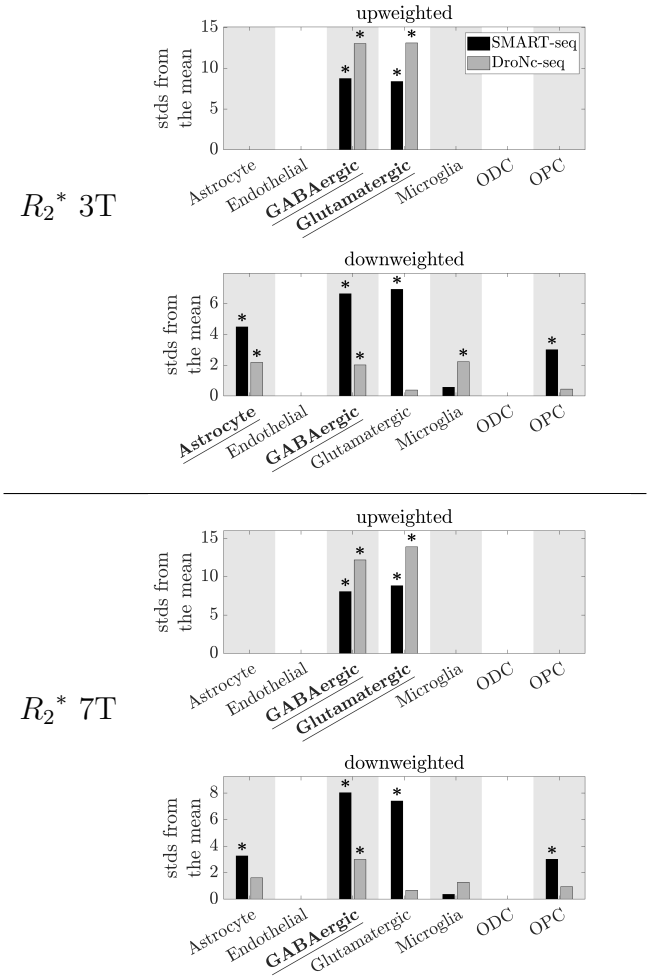

Figure 3: EWCE results showing the cell type associations of the top 5% of genes associated with R_2* at 3T and 7T (first PLS component only). Plotted are the number of standard deviations (stds) by which the EWCE value deviated from the mean value over bootstrapped target lists. Results from the two cell type-specific datasets are plotted in different colours: SMART-seq in black, DroNc-seq in grey. Top: 3T. Bottom: 7T. Bars are only plotted when FDR-corrected $p < 0.5$. *: FDR-corrected $p < 0.05$. Significant cell type associations which replicated between both cell type-specific datasets (robust results) are underlined and in bold.

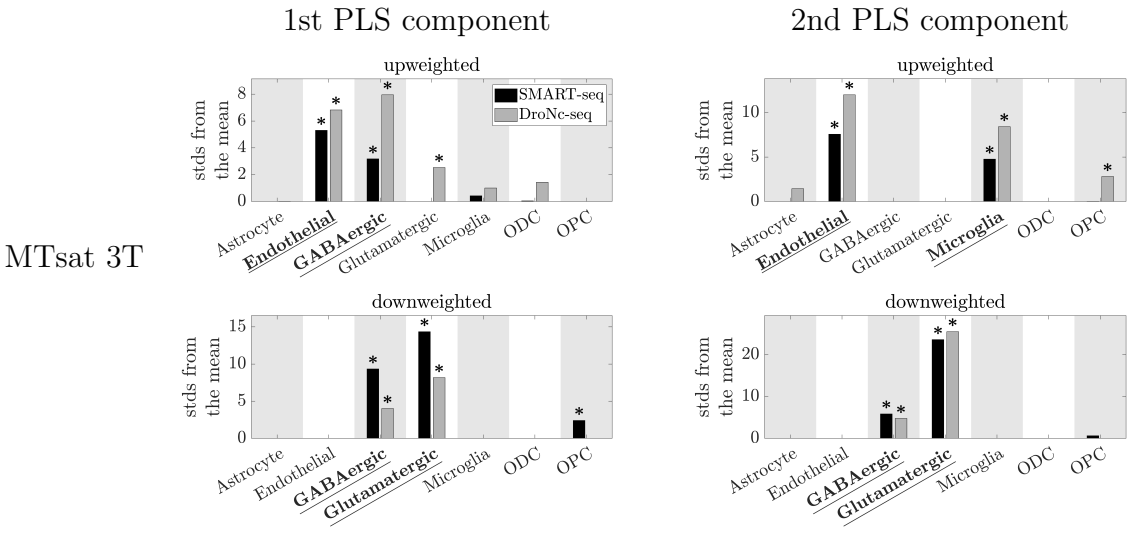

Figure 4: EWCE results showing the cell type associations of the top 5% of genes associated with MTsat at 3T. Plotted are the number of standard deviations (stds) by which the EWCE value deviated from the mean value over bootstrapped target lists. Results from the two cell type-specific datasets are plotted in different colours: SMART-seq in black, DroNc-seq in grey. Left: First component of the PLS. Right: Second component of the PLS. Bars are only plotted when FDR-corrected $p < 0.5$. *: FDR-corrected $p < 0.05$. Significant cell type associations which replicated between both cell type-specific datasets (robust results) are underlined and in bold.

DroNc-seq dataset, respectively. Similarly, associations with astrocytes and OPCs were also seen at the top 5% level in the DroNc-seq dataset for the second PLS component, but these only replicated at the top 20% (Figure S9) and top 10% (Figure S8) levels, respectively, in the SMART-seq dataset.

The 7T R_1 associations differed from the 3T results. Robust associations were seen with astrocytes, GABAergic neurons, glutamatergic neurons, microglia, and ODCs (Figures 2 and 5). Further associations with endothelial cells and OPCs were seen at the top 5% level in the DroNc-seq dataset, but these only replicated at the top 20% in the SMART-seq dataset (Figures S3 and S9).

The results after excluding regions potentially strongly affected by B_1 and B_0 artefacts from the 7T R_1 data (the orbitofrontal complex and area TE2 anterior (Glasser et al., 2016)) can be found in the Supplementary Material. Excluding these regions resulted in a decrease in the variance explained in R_1 by the first PLS component, but an increase in the variance explained by the second PLS component (Table S1), such that overall

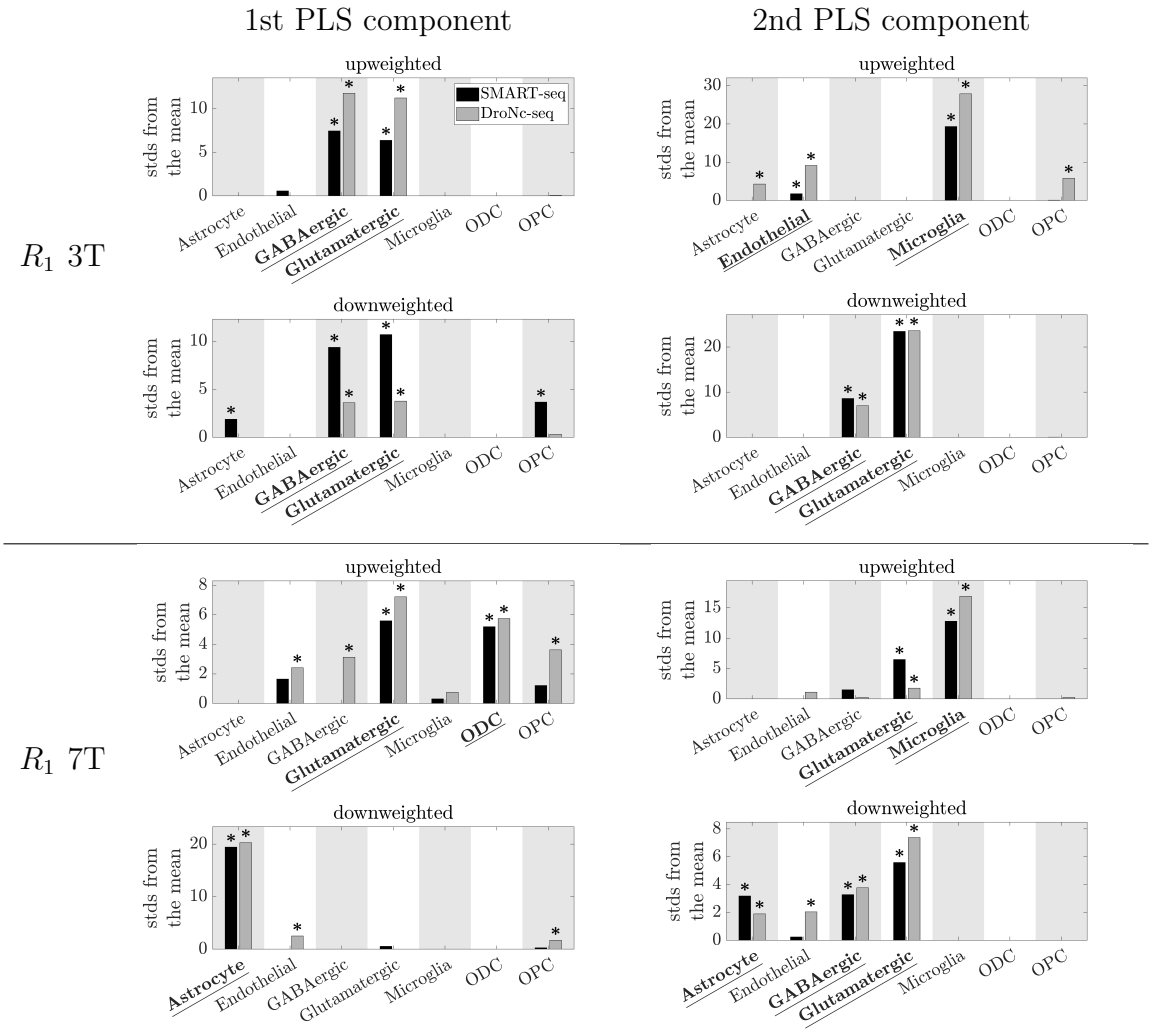

Figure 5: EWCE results showing the cell type associations of the top 5% of genes associated with R_1 at 3T and 7T. Plotted are the number of standard deviations (stds) by which the EWCE value deviated from the mean value over bootstrapped target lists. Results from the two cell type-specific datasets are plotted in different colours: SMART-seq in black, DroNc-seq in grey. Top: 3T. Bottom: 7T. Left: First component of the PLS. Right: Second component of the PLS. Bars are only plotted when FDR-corrected $p < 0.5$. *: FDR-corrected $p < 0.05$. Significant cell type associations which replicated between both cell type-specific datasets (robust results) are underlined and in bold.

the variance explained in R_1 by the two components increased. There were some changes in the cell type associations (Figure S13): a robust association with genes enriched in GABAergic neurons was seen in both PLS components compared to only in the second PLS component, and a robust association with genes enriched in OPCs was seen in the second PLS component which was not present in the previous results (cf. Figures 2 and 5). The full R_1 EWCE results after excluding potentially strongly affected regions can be found in Figures S14 and S15.

Discussion

The EWCE results showed robust associations of excitatory and inhibitory neurons with all qMRI parameters under consideration at both 3T and 7T, implying that neurons are (i.e. cytoarchitecture is) the main predictor of these cortical qMRI contrasts. This observation is in line with previous observations of general cortical gradients between sensorimotor and higher areas in many different modalities (Huntenburg et al., 2018), which are also visible in Figure 1. In addition, $R_2{}^*$ at 3T showed robust associations with astrocytes; MTsat at 3T showed robust associations with endothelial cells and microglia; R_1 at 3T showed robust associations with microglia and endothelial cells; and R_1 at 7T showed robust associations with microglia, ODCs, and astrocytes.

Figure 2 gives a visual impression of the associations. It shows that while the qMRI parameters are highly correlated – as would be expected due to their dependence on the same underlying biological substrate – they are not identical in their associations. The differential associations of the spatial distribution of the qMRI parameters with different cell types implies that by combining them, we could become sensitive to specific cell types. As an example, combination of $R_2{}^*$ at 3T and at 7T could potentially allow inference of the spatial distribution of astrocytes, as despite otherwise similar associations, R_1 at 3T is robustly associated with astrocytes, but $R_2{}^*$ at 7T is not. This presents an interesting direction for future research. Figure 2 is intended to allow other such parameter combinations to be easily read off.

The regional distribution of R_2^* in the cortex was robustly associated with excitatory and inhibitory (GABAergic) neurons, and this association was very consistent between field strengths. This association is in line with the observations by McColgan et al. (2021) at 7T (who linked cytoarchitecture from post-mortem histology to the same 7T data as used here) and by Wen et al. (2018) at 3T, providing further evidence that cortical R_2^* is sensitive to neuron density (Zhao et al., 2016). The relationship to cytoarchitecture suggests an indirect link to myelin, as local neurons are both the source of local myelinated axons (Braitenberg, 1962; Hellwig, 1993; Dinse et al., 2015; Micheva et al., 2018), and their dendrites are the target of remote axons entering the cortex. However the existence of general cortical gradients (Huntenburg et al., 2018) make the direction of the effect difficult to determine.

We did not see robust associations of R_2^* with endothelial cells or some of the glia types (microglia and OPCs) observed by Wen et al. (2018), though we did see an association with astrocytes at 3T, which could reflect the sensitivity of R_2^* to iron (Edwards et al., 2018; Möller et al., 2019). We note, however, that associations with microglia (3T) and OPCs (3T and 7T) were each significant in one of the two cell type-specific datasets (Figure 2).

The lack of robust associations of R_2^* with endothelial cells, microglia and OPCs is potentially because our algorithm to estimate R_2^* differed significantly from that in Wen et al. (2018). Wen et al. (2018) used the extensive range of echo times in their MRI protocol to separate the signal decay into fast relaxing (interpreted as vascular) and slow relaxing (interpreted as tissue) components (Ulrich and Yablonskiy, 2016), while we assumed a common single exponential R_2^* decay between the weighted images (Weiskopf et al., 2014), allowing robust estimation of R_2^* over the smaller set of echo times in our higher-resolution (thus lower signal-to-noise ratio [SNR]) data. The assumption of single exponential decay will mix decay rates of the slow and fast relaxing components; on top of this, the assumption of a common R_2^* decay between different weightings can break down in complex multi-compartment systems like brain tissue (Chan and Marques, 2020). Unfortunately, neither our 3T nor our 7T protocol allows us to apply the algorithm used

by Wen et al. (2018) to explore this further.

MTsat is commonly interpreted as representing macromolecular content, as it cleanly differentiates between GM, WM, and cerebrospinal fluid (Helms et al., 2008; Callaghan et al., 2015) and correlates with post mortem tissue metrics of myelin (Georgiadis et al., 2021), one of the largest sources of macromolecules in the brain. Interestingly, MTsat did not show robust associations with ODCs or OPCs (which would represent a direct relation to myelin), but was robustly associated with genes enriched in excitatory and inhibitory neurons, i.e. cytoarchitecture, like $R_2{}^*$, suggesting a potential indirect link to myelin. It should also be noted that there is significant cortical macromolecular content that is not associated with myelin (Mezer et al., 2013), which would not be captured by ODC and OPC associations.

The robust association of MTsat with genes enriched in endothelial cells suggests an association with cortical vasculature, as these cells line the walls of blood vessels (Duvernoy et al., 1981). A relationship between MTsat and vasculature is surprising when one considers the interpretation of MTsat as a myelin marker. One possible explanation is that the macromolecules in the endothelial cells could give rise to an observable MT effect. Another explanation could be a mechanism of magnetization transfer studied in the context of functional MRI (Pike et al., 1992; Kim et al., 2008; Schulz et al., 2020). In short, off-resonance MT-saturation pulses can efficiently saturate the water spins in cortical tissue, but not those in blood. Perfusion of this non-saturated blood into the saturated tissue via capillaries will give a local increase in signal, with the amount of perfused blood and thus the signal increasing proportionally to the amount of local vascularisation. As the amount of local vascularisation is spatially varying (e.g. primary cortical areas have a highly vascularised layer IV (Schmid et al., 2019)), this could give rise to spatial variance in MTsat, explaining the observed relationship between MTsat and endothelial cells. Relatedly, the robust association of MTsat with microglia could be due to "off-resonance saturation" (Zurkiya and Hu, 2006; Delangre et al., 2015; Bossoni et al., 2022) in the neighbourhood of iron-rich microglia. Off-resonance saturation has been shown to be additive to the MT effect (Zurkiya and Hu, 2006; Delangre et al.,

2015).

Like for $R_2{}^*$, the regional distribution of R_1 at both 3T and 7T was robustly associated with genes enriched in excitatory (glutamatergic) and inhibitory (GABAergic) neurons. The similarity of the R_1 associations to those of $R_2{}^*$ was particularly strong at 3T (compare Figures 3 and 5).

In addition to the neuronal associations, R_1 at 3T was robustly associated with gene expression associated with endothelial cells and microglia, showing similarity to the MTsat results. A similarity between R_1 and MTsat results is expected because of MT contributions to R_1 modulated by the excitation pulse (Teixeira et al., 2019; Olsson et al., 2020). However the associations could alternatively be due to iron-induced contributions (Rooney et al., 2007; Stüber et al., 2014) to the R_1 (Möller et al., 2019).

R_1 at 7T showed, in addition to the neuronal associations, robust associations with genes enriched in astrocytes and microglia, which could, like similar associations at 3T, reflect iron-induced contributions to the relaxation (Möller et al., 2019); the lack of the astrocyte association at 3T and the endothelial cell association at 7T could suggest a magnetic field strength dependence of the relaxation contributions from these cell types. It should be noted, however, that the magnetic field strength dependence of iron contributions to R_1 is expected to be small (Rooney et al., 2007; Wang et al., 2020).

The regional distribution of R_1 at 7T was also robustly associated with genes enriched in ODCs. This is consistent with the use of 7T R_1 as a cortical myelin marker (Edwards et al., 2018), though it should be noted that ODCs are also iron rich (Möller et al., 2019), and myelin and iron concentration are correlated (Kirilina et al., 2020).

Our observation of a robust association of R_1 at 7T with ODCs suggests that R_1 at 7T could be more sensitive to myelin than at 3T. This appears to contradict to the results of Rooney et al. (2007) and Wang et al. (2020), who found that the contribution of myelin to R_1 decreases going from 3T to 7T. However the analysis of Wang et al. (2020) did show that going from 3T to 7T increases the MT with the macromolecular pool; this MT increase could explain the increased apparent myelin sensitivity, as our R_1 estimates are affected by MT (Teixeira et al., 2019; Olsson et al., 2020). It should be noted that this

assessment is somewhat contradicted by the MTsat results (Figure 4) being more similar to the 3T than the 7T R_1 results (Figure 5).

The observation of a robust association of R_1 with endothelial cells at 3T but not at 7T could be due to relative changes in the R_1 of grey matter and venous blood with magnetic field strength, which, based on literature values of the respective R_1 values (Deistung et al., 2008), would lead to a relative decrease in the contribution of blood going from 3T to 7T. However, we cannot rule out that it could also be due to differences in the contribution of flow artefacts. These are likely to be more prevalent in the 7T data because while at 3T the scanner's RF body coil was used for excitation, giving spatially non-selective spin excitation over a large region, at 7T a head-only RF transmit coil was used, meaning spin excitation was more localised. The localised transmission means that spins in the blood flowing into the brain are not excited: the effects of in-flow from these non-excited spins could blur the image contrast by giving rise to a spatially-differentiated increase in physiological noise correlated with spatial variations in cortical vascularisation.

It is of interest to note that the spatial distribution of the score vectors of the (gene $\times$ RoI) matrix of the first and second PLS components of R_1 and MTsat at 3T show similar spatial patterns (Figure 1), following the general gradient observed in neuroimaging (Huntenburg et al., 2018; Goulas et al., 2021). This stands in contrast to the score vector of the second PLS component of the R_1 at 7T, which is visibly different with an apparent superior–inferior gradient. The difference in the spatial distributions of the second PLS component could give clues to the source of the differences, but could also be a result of this component reflecting stronger B_1 and B_0 artefacts at 7T compared to 3T (Hoult, 2000; Van de Moortele et al., 2002; Stockmann and Wald, 2018).

To investigate the possibility that artefacts at 7T drive our results, we repeated the 7T R_1 analysis excluding regions expected to be potentially affected. This did give rise to an increase in the variance explained by the first two PLS components, suggesting that in so doing we removed a source of variance that could not be explained using the gene expression distribution, i.e. that these areas were affected by artefacts. Exclusion of these regions did not result in removing any of the robust cell type associations, however. The

only difference was that in this case R_1 was also robustly associated with genes enriched in OPCs, in line with cortical R_1 at 7T reflecting myelin.

The 3T results for MTsat and R_1 deviated from the results for MTR and R_1 in Patel et al. (2020). As the dataset used here gave results comparable to Patel et al. (2020) when using a similar pipeline to the one they used (Edwards et al., 2019), we can attribute the discrepancy to the different analysis pipeline used here. The two major differences (although other differences such as gene normalisation could also play a role (Markello et al., 2021)) were that we used (1) a finer cortical atlas (180 cortical areas vs. 34) and (2) human-derived gene lists (Habib et al., 2017; Hodge et al., 2019) rather than mouse-derived lists (Zeisel et al., 2015).

(1) The sampling density of gene expression over the cortical surfaces in the AHBA is relatively sparse, and so averaging expression levels over regions of interest (RoIs) helps to increase the robustness of the results (Arnatkevičiūtė et al., 2019). If the RoIs are too large, however, then spatial specificity is lost, as functionally and anatomically distinct cortical areas get merged together. The HCP-MMP1.0 atlas is derived based on boundaries found from in vivo anatomical and functional MRI data (Glasser et al., 2016), allowing reasonable specificity, while the RoIs are sufficiently large that a reasonable mapping to the gene expression samples in the AHBA atlas is possible (Arnatkevičiūtė et al., 2019).

(2) Mouse-derived cell type-specific gene expression has been found to be less able to discriminate cell types in human because of species-specific features, especially for non-neuronal cell types (Hodge et al., 2019). Human-derived lists should thus be preferred where possible.

Limitations

The investigated qMRI parameters have previously been shown to exhibit a dependence on the orientation of the brain microstructure with respect to the static magnetic field of the scanner (Cohen-Adad et al., 2012; Pampel et al., 2015; Schyboll et al., 2020). This is because the microscopic myelin distribution in cortex is relatively ordered, with

most myelinated axons running either tangentially or radially with respect to the cortical surface (Edwards et al., 2018). This regular structure can give rise to an orientation dependence of the quantitative parameters, which for $R_2{}^*$ arises from the anisotropic susceptibility distribution of myelin (Bender and Klose, 2010; Cohen-Adad et al., 2012) and for R_1 and MTsat arises from the anisotropic tumbling of water bound to myelin which is mediated by the oriented nature of lipid bilayers of the myelin sheaths (Pampel et al., 2015; Schyboll et al., 2020). As the former mechanism depends on susceptibility, we would expect the orientation dependence to scale with field strength. However, the similarity of our $R_2{}^*$ results at 3T and 7T would suggest that this effect does not play a major role in our analysis. The absence of this effect is likely because the averaging over cortical areas also averages over cortex oriented at a range of angles; this averaging will also have reduced orientation effects in the other parameters.

The first PLS component explained the majority of the variance in the spatial distribution of $R_2{}^*$ at 3T and 7T and R_1 at 3T, while a second PLS component was additionally needed to explain the majority of the variance in MTsat. In the case of R_1 at 7T, however, the explained variance was still not over 50%, implying that there could be major sources of variance (e.g. additional cell types or imaging artefacts) that are important for the spatial contrast distribution in this case which are not included in our model. Excluding potentially artefact-affected areas from the 7T R_1 analysis increased the variance explained slightly (compare Tables 1 and S1), in line with this hypothesis (as the spatial distribution of imaging artefacts will not be explicable in terms of cell types), but the variance explained still did not reach 50%.

We only examined associations with MRI parameters sampled on the central cortical surface. This choice was made to exclude as far as possible the contribution of partial volume effects with the white matter and CSF when comparing between the 3T and 7T data, and thus mitigate any confounding effects from the lower resolution of the 3T data. Our previous work using the 7T data presented here has shown that across the depth of the cortex $R_2{}^*$ (but not R_1) has strong associations with genes specific to cytoarchitectonic cortical layers II, III, IV and V (McColgan et al., 2021).

Our test of the association of MPMs with cell types is indirect, relying on the cell type-specificity of genes. Future analyses could refine the analysis by including maps of neurotransmitter receptors (Dukart et al., 2021; Goulas et al., 2021), as these could give greater specificity when testing the associations with neurons.

Our in vivo data comes from young adults. In contrast, the post mortem gene expression atlases and cell type-specific gene expression datasets come from donors with a broader range of ages, most of which are older than our subjects (Hawrylycz et al., 2015; Habib et al., 2017; Hodge et al., 2019). During the mapping of gene expression from the AHBA donor datasets to the HCP-MMP1.0 atlas (Arnatkevičiūtė et al., 2019), the genes were filtered based on differential stability to mitigate subject-specific effects (Hawrylycz et al., 2015). However, as the cortical cell distribution (e.g. of glia) is dynamic (Edwards et al., 2018; Arnatkevičiūtė et al., 2019; Marsh et al., 2022), the regional gene expression atlas may not be entirely representative of our cohort. This could potentially affect the sensitivity of the method to individual cell types. It should be noted, though, that regional variation in cortical gene expression has previously been found to be relatively conserved between individuals (Hawrylycz et al., 2015).

Our results suggest that interareal-variations in MPMs largely reflect differences in gene expression associated with neurons, i.e. with cytoarchitecture. These results are however not necessarily applicable to longitudinal or inter-subject/-group comparisons, which can give rise to different associations. An example is provided by Patel et al. (2019): their gene expression analysis results showed that while the spatial distribution of MTR was not significantly associated with ODCs at either age 14 or five years later at age 19, the change in MTR between the two time points was significantly associated with ODCs. The results presented here imply that it would be interesting to examine such cases using the broad range of qMRI parameters and static magnetic field strengths examined here.

Conclusions

The spatial distribution of all of the quantitative MRI parameters at both 3T and 7T robustly covaried with the distribution of genes enriched in neurons. This reflects the

importance of cytoarchitecture in determining MRI contrast.

In addition to the general association with neurons, the spatial distribution of the parameters was found to robustly covary with the distribution of genes enriched in astrocytes (R_2^* at 3T, R_1 at 7T), endothelial cells (R_1 and MTsat at 3T), microglia (R_1 and MTsat at 3T, R_1 at 7T), and ODCs (R_1 at 7T). As the differences in spatial distributions of the parameters were associated with different cell types, these results imply it may be possible to extract information about individual cell types by combining the quantitative parameters.

The results complement the traditional interpretation of qMRI parameters in terms of iron and myelin, and advance the possible use of qMRI parameters as biomarkers for specific cell types, bringing us closer to the goal of in vivo histology using MRI.

Funding

This work was supported by the European Research Council under the European Union's Seventh Framework Programme (FP7/2007-2013)/ERC (grant number 616905); and the European Union's Horizon 2020 research and innovation programme / the European Research Council (grant number 681094).

Conflicts of Interest

The Max Planck Institute for Human Cognitive and Brain Sciences has an institutional research agreement with Siemens Healthcare. NW holds a patent on acquisition of MRI data during spoiler gradients (US 10,401,453 B2). NW was a speaker at an event organized by Siemens Healthcare and was reimbursed for the travel expenses.

References

Abdi, H., 2010. Partial least squares regression and projection on latent structure regression (PLS regression). WIREs Computational Statistics 2, 97–106. doi:10.1002/wics.51.

Arnatkevičiūtė, A., Fulcher, B.D., Fornito, A., 2019. A practical guide to linking brain-wide gene expression and neuroimaging data. NeuroImage 189, 353–367. doi:10.1016/j.neuroimage.2019.01.011.

Bender, B., Klose, U., 2010. The in vivo influence of white matter fiber orientation towards B0 on T2* in the human brain. NMR in Biomedicine 23, 1071–1076. doi:10.1002/nbm.1534.

Bonaiuto, J.J., Meyer, S.S., Little, S., Rossiter, H., Callaghan, M.F., Dick, F., Barnes, G.R., Bestmann, S., 2018. Lamina-specific cortical dynamics in human visual and sensorimotor cortices. eLife 7, e33977. doi:10.7554/eLife.33977.

Bossoni, L., Hegeman-Kleinn, I., van Duinen, S.G., Bulk, M., Vroegindeweij, L.H.P., Langendonk, J.G., Hirschler, L., Webb, A., van der Weerd, L., 2022. Off-resonance saturation as an MRI method to quantify mineral-iron in the post-mortem brain. Magnetic Resonance in Medicine 87, 1276–1288. doi:10.1002/mrm.29041.

Braitenberg, V., 1962. A note on myeloarchitectonics. Journal of Comparative Neurology 118, 141–156. doi:10.1002/cne.901180202.

Callaghan, M.F., Helms, G., Lutti, A., Mohammadi, S., Weiskopf, N., 2015. A general linear relaxometry model of R_1 using imaging data. Magnetic Resonance in Medicine 73, 1309–1314. doi:10.1002/mrm.25210.

Carey, D., Caprini, F., Allen, M., Lutti, A., Weiskopf, N., Rees, G., Callaghan, M.F., Dick, F., 2018. Quantitative MRI provides markers of intra-, inter-regional, and age-related differences in young adult cortical microstructure. NeuroImage 182, 429–440. doi:10.1016/j.neuroimage.2017.11.066.

Chan, K.S., Marques, J.P., 2020. Multi-compartment relaxometry and diffusion informed myelin water imaging – promises and challenges of new gradient echo myelin water imaging methods. NeuroImage 221, 117159. doi:10.1016/j.neuroimage.2020.117159.

CJ Neurolab, 2018. HCP-MMP1.0 volumetric (NIfTI) masks in native structural space. doi:10.6084/m9.figshare.4249400.v5. figshare. Dataset.

Cohen-Adad, J., Polimeni, J.R., Helmer, K.G., Benner, T., McNab, J.A., Wald, L.L., Rosen, B.R., Mainero, C., 2012. T_2^* mapping and B_0 orientation-dependence at 7 T reveal cyto- and myeloarchitecture organization of the human cortex. NeuroImage 60, 1006–1014. doi:10.1016/j.neuroimage.2012.01.053.

Collins, C.M., Liu, W., Wang, J., Gruetter, R., Vaughan, J.T., Ugurbil, K., Smith, M.B., 2004. Temperature and SAR calculations for a human head within volume and surface coils at 64 and 300 MHz. Journal of Magnetic Resonance Imaging 19, 650–656. doi:10.1002/jmri.20041.

Deistung, A., Rauscher, A., Sedlacik, J., Stadler, J., Witoszynskyj, S., Reichenbach, J.R., 2008. Susceptibility weighted imaging at ultra high magnetic field strengths: Theoretical considerations and experimental results. Magnetic Resonance in Medicine 60, 1155–1168. doi:10.1002/mrm.21754.

Delangre, S., Vuong, Q.L., Henrard, D., Po, C., Gallez, B., Gossuin, Y., 2015. Bottom-up study of the MRI positive contrast created by the Off-Resonance Saturation sequence. Journal of Magnetic Resonance 254, 98–109. doi:10.1016/j.jmr.2015.02.014.

Dinse, J., Härtwich, N., Waehnert, M.D., Tardif, C.L., Schäfer, A., Geyer, S., Preim, B., Turner, R., Bazin, P., 2015. A cytoarchitecture-driven myelin model reveals area-specific signatures in human primary and secondary areas using ultra-high resolution in-vivo brain MRI. NeuroImage 114, 71–87. doi:10.1016/j.neuroimage.2015.04.023.

Dukart, J., Holiga, S., Rullmann, M., Lanzenberger, R., Hawkins, P.C.T., Mehta, M.A., Hesse, S., Barthel, H., Sabri, O., Jech, R., Eickhoff, S.B., 2021. JuSpace: A tool for

spatial correlation analyses of magnetic resonance imaging data with nuclear imaging derived neurotransmitter maps. Human Brain Mapping 42, 555–566. doi:10.1002/hbm.25244.

Duvernoy, H.M., Delon, S., Vannson, J.L., 1981. Cortical blood vessels of the human brain. Brain Research Bulletin 7, 519–579. doi:10.1016/0361-9230(81)90007-1.

Edwards, L.J., Kirilina, E., Mohammadi, S., Weiskopf, N., 2018. Microstructural imaging of human neocortex in vivo. NeuroImage 182, 184–206. doi:10.1016/j.neuroimage.2018.02.055.

Edwards, L.J., McColgan, P., Helbling, S., Dick, F., Weiskopf, N., 2019. Quantitative MRI maps of human neocortex explored using cell-specific gene expression analysis, in: OHBM Annual Meeting 2019, p. 1133.

Fischl, B., van der Kouwe, A., Destrieux, C., Halgren, E., Ségonne, F., Salat, D.H., Busa, E., Seidman, L.J., Goldstein, J., Kennedy, D., Caviness, V., Makris, N., Rosen, B., Dale, A.M., 2004. Automatically parcellating the human cerebral cortex. Cerebral Cortex 14, 11–22. doi:10.1093/cercor/bhg087.

Fornito, A., Arnatkevičiūtė, A., Fulcher, B.D., 2019. Bridging the gap between Connectome and Transcriptome. Trends in Cognitive Sciences 23, 34–50. doi:10.1016/j.tics.2018.10.005.

Georgiadis, M., Schroeter, A., Gao, Z., Guizar-Sicairos, M., Liebi, M., Leuze, C., McNab, J.A., Balolia, A., Veraart, J., Ades-Aron, B., Kim, S., Shepherd, T., Lee, C.H., Walczak, P., Chodankar, S., DiGiacomo, P., David, G., Augath, M., Zerbi, V., Sommer, S., Rajkovic, I., Weiss, T., Bunk, O., Yang, L., Zhang, J., Novikov, D.S., Zeineh, M., Fieremans, E., Rudin, M., 2021. Nanostructure-specific X-ray tomography reveals myelin levels, integrity and axon orientations in mouse and human nervous tissue. Nature Communications 12, 2941. doi:10.1038/s41467-021-22719-7.

Glasser, M.F., Coalson, T.S., Robinson, E.C., Hacker, C.D., Harwell, J., Yacoub, E., Ugurbil, K., Andersson, J., Beckmann, C.F., Jenkinson, M., Smith, S.M., Van Essen,

D.C., 2016. A multi-modal parcellation of human cerebral cortex. Nature 536, 171–178. doi:10.1038/nature18933.

Goulas, A., Changeux, J.P., Wagstyl, K., Amunts, K., Palomero-Gallagher, N., Hilgetag, C.C., 2021. The natural axis of transmitter receptor distribution in the human cerebral cortex. Proceedings of the National Academy of Sciences 118, e2020574118. doi:10.1073/pnas.2020574118.

Griswold, M.A., Jakob, P.M., Heidemann, R.M., Nittka, M., Jellus, V., Wang, J., Kiefer, B., Haase, A., 2002. Generalized autocalibrating partially parallel acquisitions (GRAPPA). Magnetic Resonance in Medicine 47, 1202–1210. doi:10.1002/mrm.10171.

Habib, N., Avraham-Davidi, I., Basu, A., Burks, T., Shekhar, K., Hofree, M., Choudhury, S.R., Aguet, F., Gelfand, E., Ardlie, K., Weitz, D.A., Rozenblatt-Rosen, O., Zhang, F., Regev, A., 2017. Massively parallel single-nucleus RNA-seq with DroNc-seq. Nature Methods 14, 955–958. doi:10.1038/nmeth.4407.

Hawrylycz, M., Miller, J.A., Menon, V., Feng, D., Dolbeare, T., Guillozet-Bongaarts, A.L., Jegga, A.G., Aronow, B.J., Lee, C.K., Bernard, A., Glasser, M.F., Dierker, D.L., Menche, J., Szafer, A., Collman, F., Grange, P., Berman, K.A., Mihalas, S., Yao, Z., Stewart, L., Barabási, A.L., Schulkin, J., Phillips, J., Ng, L., Dang, C., Haynor, D.R., Jones, A., Van Essen, D.C., Koch, C., Lein, E., 2015. Canonical genetic signatures of the adult human brain. Nature Neuroscience 18, 1832–1844. doi:10.1038/nn.4171.

Hawrylycz, M.J., Lein, E.S., Guillozet-Bongaarts, A.L., Shen, E.H., Ng, L., Miller, J.A., van de Lagemaat, L.N., Smith, K.A., Ebbert, A., Riley, Z.L., Abajian, C., Beckmann, C.F., Bernard, A., Bertagnolli, D., Boe, A.F., Cartagena, P.M., Chakravarty, M.M., Chapin, M., Chong, J., Dalley, R.A., Daly, B.D., Dang, C., Datta, S., Dee, N., Dolbeare, T.A., Faber, V., Feng, D., Fowler, D.R., Goldy, J., Gregor, B.W., Haradon, Z., Haynor, D.R., Hohmann, J.G., Horvath, S., Howard, R.E., Jeromin, A., Jochim, J.M., Kinnunen, M., Lau, C., Lazarz, E.T., Lee, C., Lemon, T.A., Li, L., Li, Y., Morris, J.A., Overly, C.C., Parker, P.D., Parry, S.E., Reding, M., Royall, J.J., Schulkin,

J., Sequeira, P.A., Slaughterbeck, C.R., Smith, S.C., Sodt, A.J., Sunkin, S.M., Swanson, B.E., Vawter, M.P., Williams, D., Wohnoutka, P., Zielke, H.R., Geschwind, D.H., Hof, P.R., Smith, S.M., Koch, C., Grant, S.G.N., Jones, A.R., 2012. An anatomically comprehensive atlas of the adult human brain transcriptome. Nature 489, 391–399. doi:10.1038/nature11405.

Hellwig, B., 1993. How the myelin picture of the human cerebral cortex can be computed from cytoarchitectural data. A bridge between von Economo and Vogt. Journal für Hirnforschung 34, 387–402.

Helms, G., Dathe, H., Kallenberg, K., Dechent, P., 2008. High-resolution maps of magnetization transfer with inherent correction for RF inhomogeneity and T1 relaxation obtained from 3D FLASH MRI. Magnetic Resonance in Medicine 60, 1396–1407. doi:10.1002/mrm.21732. erratum: Helms et al. (2010).

Helms, G., Dathe, H., Kallenberg, K., Dechent, P., 2010. Erratum to: Helms, Dathe, Kallenberg and Dechent, High-resolution maps of magnetization transfer with inherent correction for RF inhomogeneity and T1 relaxation obtained from 3D FLASH MRI. Magn Reson Med 2008 Dec; 60(6):1396–1407. Magnetic Resonance in Medicine 64, 1856–1856. doi:https://doi.org/10.1002/mrm.22607.

Hodge, R.D., Bakken, T.E., Miller, J.A., Smith, K.A., Barkan, E.R., Graybuck, L.T., Close, J.L., Long, B., Johansen, N., Penn, O., Yao, Z., Eggermont, J., Höllt, T., Levi, B.P., Shehata, S.I., Aevermann, B., Beller, A., Bertagnolli, D., Brouner, K., Casper, T., Cobbs, C., Dalley, R., Dee, N., Ding, S.L., Ellenbogen, R.G., Fong, O., Garren, E., Goldy, J., Gwinn, R.P., Hirschstein, D., Keene, C.D., Keshk, M., Ko, A.L., Lathia, K., Mahfouz, A., Maltzer, Z., McGraw, M., Nguyen, T.N., Nyhus, J., Ojemann, J.G., Oldre, A., Parry, S., Reynolds, S., Rimorin, C., Shapovalova, N.V., Somasundaram, S., Szafer, A., Thomsen, E.R., Tieu, M., Quon, G., Scheuermann, R.H., Yuste, R., Sunkin, S.M., Lelieveldt, B., Feng, D., Ng, L., Bernard, A., Hawrylycz, M., Phillips, J.W., Tasic, B., Zeng, H., Jones, A.R., Koch, C., Lein, E.S., 2019. Conserved cell types

with divergent features in human versus mouse cortex. Nature 573, 61–68. doi:10.1038/s41586-019-1506-7.

Hoult, D.I., 2000. Sensitivity and power deposition in a high-field imaging experiment. Journal of Magnetic Resonance Imaging 12, 46–67. doi:10.1002/1522-2586(200007)12:1<46::AID-JMRI6>3.0.CO;2-D.

Huntenburg, J.M., Bazin, P.L., Margulies, D.S., 2018. Large-scale gradients in human cortical organization. Trends in Cognitive Sciences 22, 21–31. doi:10.1016/j.tics.2017.11.002.

Kim, T., Hendrich, K., Kim, S.G., 2008. Functional MRI with magnetization transfer effects: Determination of BOLD and arterial blood volume changes. Magnetic Resonance in Medicine 60, 1518–1523. doi:10.1002/mrm.21766.

Kirilina, E., Helbling, S., Morawski, M., Pine, K., Reimann, K., Jankuhn, S., Dinse, J., Deistung, A., Reichenbach, J.R., Trampel, R., Geyer, S., Müller, L., Jakubowski, N., Arendt, T., Bazin, P.L., Weiskopf, N., 2020. Superficial white matter imaging: Contrast mechanisms and whole-brain in vivo mapping. Science Advances 6, eaaz9281. doi:10.1126/sciadv.aaz9281.

Krishnan, A., Williams, L.J., McIntosh, A.R., Abdi, H., 2011. Partial least squares (PLS) methods for neuroimaging: A tutorial and review. NeuroImage 56, 455–475. doi:10.1016/j.neuroimage.2010.07.034.

Langkammer, C., Krebs, N., Goessler, W., Scheurer, E., Ebner, F., Yen, K., Fazekas, F., Ropele, S., 2010. Quantitative MR imaging of brain iron: A postmortem validation study. Radiology 257, 455–462. doi:10.1148/radiol.10100495.

Lein, E.S., Belgard, T.G., Hawrylycz, M., Molnár, Z., 2017. Transcriptomic perspectives on neocortical structure, development, evolution, and disease. Annual Review of Neuroscience 40, 629–652. doi:10.1146/annurev-neuro-070815-013858.

Lent, R., Azevedo, F.A.C., Andrade-Moraes, C.H., Pinto, A.V.O., 2012. How many neurons do you have? Some dogmas of quantitative neuroscience under revision. European Journal of Neuroscience 35, 1–9. doi:10.1111/j.1460-9568.2011.07923.x.

Leutritz, T., Seif, M., Helms, G., Samson, R.S., Curt, A., Freund, P., Weiskopf, N., 2020. Multiparameter mapping of relaxation (R1, R2*), proton density and magnetization transfer saturation at 3 T: A multicenter dual-vendor reproducibility and repeatability study. Human Brain Mapping 41, 4232–4247. doi:10.1002/hbm.25122.

Liu, S., Li, A., Zhu, M., Li, J., Liu, B., 2019. Genetic influences on cortical myelination in the human brain. Genes, Brain and Behavior 18, e12537. doi:10.1111/gbb.12537.

Lutti, A., Hutton, C., Finsterbusch, J., Helms, G., Weiskopf, N., 2010. Optimization and validation of methods for mapping of the radiofrequency transmit field at 3T. Magnetic Resonance in Medicine 64, 229–238. doi:10.1002/mrm.22421.

Lutti, A., Stadler, J., Josephs, O., Windischberger, C., Speck, O., Bernarding, J., Hutton, C., Weiskopf, N., 2012. Robust and fast whole brain mapping of the RF transmit field B1 at 7T. PLOS ONE 7, 1–7. doi:10.1371/journal.pone.0032379.

Maggioni, M., Katkovnik, V., Egiazarian, K., Foi, A., 2013. Nonlocal transform-domain filter for volumetric data denoising and reconstruction. IEEE Transactions on Image Processing 22, 119–133. doi:10.1109/TIP.2012.2210725.

Mancini, M., Karakuzu, A., Cohen-Adad, J., Cercignani, M., Nichols, T.E., Stikov, N., 2020. An interactive meta-analysis of MRI biomarkers of myelin. eLife 9, e61523. doi:10.7554/eLife.61523.

Markello, R.D., Arnatkeviciute, A., Poline, J.B., Fulcher, B.D., Fornito, A., Misic, B., 2021. Standardizing workflows in imaging transcriptomics with the abagen toolbox. eLife 10, e72129. doi:10.7554/eLife.72129.

Marsh, S.E., Walker, A.J., Kamath, T., Dissing-Olesen, L., Hammond, T.R., de Soysa, T.Y., Young, A.M.H., Murphy, S., Abdulraouf, A., Nadaf, N., Dufort, C., Walker,

A.C., Lucca, L.E., Kozareva, V., Vanderburg, C., Hong, S., Bulstrode, H., Hutchinson, P.J., Gaffney, D.J., Hafler, D.A., Franklin, R.J.M., Macosko, E.Z., Stevens, B., 2022. Dissection of artifactual and confounding glial signatures by single-cell sequencing of mouse and human brain. Nature Neuroscience 25, 306–316. doi:10.1038/s41593-022-01022-8.

McColgan, P., Helbling, S., Vaculčiaková, L., Pine, K., Wagstyl, K., Movahedian Attar, F., Edwards, L., Papoutsi, M., Wei, Y., Van den Heuvel, M.P., Tabrizi, S.J., Rees, G., Weiskopf, N., 2021. Relating quantitative 7T MRI across cortical depths to cytoarchitectonics, gene expression and connectomics. Human Brain Mapping doi:10.1002/hbm.25595.

Mezer, A., Yeatman, J.D., Stikov, N., Kay, K.N., Cho, N.J., Dougherty, R.F., Perry, M.L., Parvizi, J., Hua, L.H., Butts-Pauly, K., Wandell, B.A., 2013. Quantifying the local tissue volume and composition in individual brains with magnetic resonance imaging. Nature Medicine 19, 1667–1672. doi:10.1038/nm.3390.

Micheva, K.D., Chang, E.F., Nana, A.L., Seeley, W.W., Ting, J.T., Cobbs, C., Lein, E., Smith, S.J., Weinberg, R.J., Madison, D.V., 2018. Distinctive structural and molecular features of myelinated inhibitory axons in human neocortex. eNeuro 5. doi:10.1523/ENEURO.0297-18.2018.

Mills, K., 2016. HCP-MMP1.0 projected on fsaverage. doi:10.6084/m9.figshare.3498446.v2. figshare. Dataset.

Möller, H.E., Bossoni, L., Connor, J.R., Crichton, R.R., Does, M.D., Ward, R.J., Zecca, L., Zucca, F.A., Ronen, I., 2019. Iron, myelin, and the brain: Neuroimaging meets neurobiology. Trends in Neurosciences 42, 384–401. doi:10.1016/j.tins.2019.03.009.

Van de Moortele, P.F., Pfeuffer, J., Glover, G.H., Ugurbil, K., Hu, X., 2002. Respiration-induced B0 fluctuations and their spatial distribution in the human brain at 7 Tesla. Magnetic Resonance in Medicine 47, 888–895. doi:10.1002/mrm.10145.

Olsson, H., Andersen, M., Lätt, J., Wirestam, R., Helms, G., 2020. Reducing bias in dual flip angle T1-mapping in human brain at 7T. Magnetic Resonance in Medicine 84, 1347–1358. doi:10.1002/mrm.28206.

Pampel, A., Müller, D.K., Anwander, A., Marschner, H., Möller, H.E., 2015. Orientation dependence of magnetization transfer parameters in human white matter. NeuroImage 114, 136–146. doi:10.1016/j.neuroimage.2015.03.068.

Patel, Y., Shin, J., Drakesmith, M., Evans, J., Pausova, Z., Paus, T., 2020. Virtual histology of multi-modal magnetic resonance imaging of cerebral cortex in young men. NeuroImage 218, 116968. doi:10.1016/j.neuroimage.2020.116968.

Patel, Y., Shin, J., Gowland, P.A., Pausova, Z., Paus, T., 2019. Maturation of the human cerebral cortex during adolescence: Myelin or dendritic arbor? Cerebral Cortex 29, 3351–3362. doi:10.1093/cercor/bhy204.

Peters, A.M., Brookes, M.J., Hoogenraad, F.G., Gowland, P.A., Francis, S.T., Morris, P.G., Bowtell, R., 2007. T2* measurements in human brain at 1.5, 3 and 7 T. Magnetic Resonance Imaging 25, 748–753. doi:10.1016/j.mri.2007.02.014. Proceedings of the International School on Magnetic Resonance and Brain Function.

Pike, G.B., Hu, B.S., Glover, G.H., Enzmann, D.R., 1992. Magnetization transfer time-of-flight magnetic resonance angiography. Magnetic Resonance in Medicine 25, 372–379. doi:10.1002/mrm.1910250217.

Romero-Garcia, R., Warrier, V., Bullmore, E.T., Baron-Cohen, S., Bethlehem, R.A.I., 2019. Synaptic and transcriptionally downregulated genes are associated with cortical thickness differences in autism. Molecular Psychiatry 24, 1053–1064. doi:10.1038/s41380-018-0023-7.

Rooney, W.D., Johnson, G., Li, X., Cohen, E.R., Kim, S.G., Ugurbil, K., Springer Jr., C.S., 2007. Magnetic field and tissue dependencies of human brain longitudinal $^{1}H_2O$ relaxation in vivo. Magnetic Resonance in Medicine 57, 308–318. doi:10.1002/mrm.21122.

Rosipal, R., Krämer, N., 2006. Overview and recent advances in partial least squares, in: Saunders, C., Grobelnik, M., Gunn, S., Shawe-Taylor, J. (Eds.), Subspace, Latent Structure and Feature Selection, Springer, Berlin, Heidelberg. pp. 34–51. doi:10.1007/11752790_2.

Schmid, F., Barrett, M.J.P., Jenny, P., Weber, B., 2019. Vascular density and distribution in neocortex. NeuroImage 197, 792–805. doi:10.1016/j.neuroimage.2017.06.046.

Schulz, J., Fazal, Z., Metere, R., Marques, J.P., Norris, D.G., 2020. Arterial blood contrast (ABC) enabled by magnetization transfer (MT): a novel MRI technique for enhancing the measurement of brain activation changes. bioRxiv doi:10.1101/2020.05.20.106666. preprint.

Schyboll, F., Jaekel, U., Petruccione, F., Neeb, H., 2020. Origin of orientation-dependent R1 (=1/T1) relaxation in white matter. Magnetic Resonance in Medicine 84, 2713–2723. doi:10.1002/mrm.28277.

Shin, J., French, L., Xu, T., Leonard, G., Perron, M., Pike, G.B., Richer, L., Veillette, S., Pausova, Z., Paus, T., 2018. Cell-specific gene-expression profiles and cortical thickness in the human brain. Cerebral Cortex 28, 3267–3277. doi:10.1093/cercor/bhx197.

Skene, N.G., Grant, S.G.N., 2016. Identification of vulnerable cell types in major brain disorders using single cell transcriptomes and expression weighted cell type enrichment. Frontiers in Neuroscience 10. doi:10.3389/fnins.2016.00016.

Stockmann, J.P., Wald, L.L., 2018. In vivo B0 field shimming methods for MRI at 7T. NeuroImage 168, 71–87. doi:10.1016/j.neuroimage.2017.06.013. neuroimaging with Ultra-high Field MRI: Present and Future.

Stüber, C., Morawski, M., Schäfer, A., Labadie, C., Wähnert, M., Leuze, C., Streicher, M., Barapatre, N., Reimann, K., Geyer, S., Spemann, D., Turner, R., 2014. Myelin and iron concentration in the human brain: A quantitative study of MRI contrast. NeuroImage 93, 95–106. doi:10.1016/j.neuroimage.2014.02.026.

Tabelow, K., Balteau, E., Ashburner, J., Callaghan, M.F., Draganski, B., Helms, G., Kherif, F., Leutritz, T., Lutti, A., Phillips, C., Reimer, E., Ruthotto, L., Seif, M., Weiskopf, N., Ziegler, G., Mohammadi, S., 2019. hMRI – a toolbox for quantitative MRI in neuroscience and clinical research. NeuroImage 194, 191–210. doi:10.1016/j.neuroimage.2019.01.029.

Teixeira, R.P.A.G., Malik, S.J., Hajnal, J.V., 2019. Fast quantitative MRI using controlled saturation magnetization transfer. Magnetic Resonance in Medicine 81, 907–920. doi:10.1002/mrm.27442.

Trampel, R., Bazin, P.L., Pine, K., Weiskopf, N., 2019. In-vivo magnetic resonance imaging (MRI) of laminae in the human cortex. NeuroImage 197, 707–715. doi:10.1016/j.neuroimage.2017.09.037.

Ulrich, X., Yablonskiy, D.A., 2016. Separation of cellular and BOLD contributions to T2* signal relaxation. Magnetic Resonance in Medicine 75, 606–615. doi:10.1002/mrm.25610.

Vaculčiaková, L., Podranski, K., Edwards, L.J., Ocal, D., Veale, T., Fox, N.C., Haak, R., Ehses, P., Callaghan, M.F., Pine, K.J., Weiskopf, N., 2022. Combining navigator and optical prospective motion correction for high-quality 500 µm resolution quantitative multi-parameter mapping at 7T. Magnetic Resonance in Medicine doi:10.1002/mrm.29253. In press.

Vértes, P.E., Rittman, T., Whitaker, K.J., Romero-Garcia, R., Váša, F., Kitzbichler, M.G., Wagstyl, K., Fonagy, P., Dolan, R.J., Jones, P.B., Goodyer, I.M., the NSPN Consortium, Bullmore, E.T., 2016. Gene transcription profiles associated with inter-modular hubs and connection distance in human functional magnetic resonance imaging networks. Philosophical Transactions of the Royal Society B: Biological Sciences 371, 20150362. doi:10.1098/rstb.2015.0362.

Wang, Y., van Gelderen, P., de Zwart, J.A., Duyn, J.H., 2020. B0-field dependence of MRI

T1 relaxation in human brain. NeuroImage 213, 116700. doi:10.1016/j.neuroimage.2020.116700.

Webb, A., 2011. Dielectric materials in magnetic resonance. Concepts in Magnetic Resonance Part A 38A, 148–184. doi:10.1002/cmr.a.20219.

Weiskopf, N., Callaghan, M.F., Josephs, O., Lutti, A., Mohammadi, S., 2014. Estimating the apparent transverse relaxation time (R2*) from images with different contrasts (ESTATICS) reduces motion artifacts. Frontiers in Neuroscience 8, 278. doi:10.3389/fnins.2014.00278.

Weiskopf, N., Edwards, L.J., Helms, G., Mohammadi, S., Kirilina, E., 2021. Quantitative magnetic resonance imaging of brain anatomy and in vivo histology. Nature Reviews Physics 3, 570–588. doi:10.1038/s42254-021-00326-1.

Weiskopf, N., Suckling, J., Williams, G., Correia, M., Inkster, B., Tait, R., Ooi, C., Bullmore, E., Lutti, A., 2013. Quantitative multi-parameter mapping of R1, PD*, MT, and R2* at 3T: a multi-center validation. Frontiers in Neuroscience 7, 95. doi:10.3389/fnins.2013.00095.

Wen, J., Goyal, M.S., Astafiev, S.V., Raichle, M.E., Yablonskiy, D.A., 2018. Genetically defined cellular correlates of the baseline brain MRI signal. Proceedings of the National Academy of Sciences 115, E9727–E9736. doi:10.1073/pnas.1808121115.

Whitaker, K.J., Vértes, P.E., Romero-Garcia, R., Váša, F., Moutoussis, M., Prabhu, G., Weiskopf, N., Callaghan, M.F., Wagstyl, K., Rittman, T., Tait, R., Ooi, C., Suckling, J., Inkster, B., Fonagy, P., Dolan, R.J., Jones, P.B., Goodyer, I.M., the NSPN Consortium, Bullmore, E.T., 2016. Adolescence is associated with genomically patterned consolidation of the hubs of the human brain connectome. Proceedings of the National Academy of Sciences 113, 9105–9110. doi:10.1073/pnas.1601745113.

Zaitsev, M., Maclaren, J., Herbst, M., 2015. Motion artifacts in MRI: A complex problem with many partial solutions. Journal of Magnetic Resonance Imaging 42, 887–901. doi:10.1002/jmri.24850.

Zarkali, A., McColgan, P., Ryten, M., Reynolds, R., Leyland, L.A., Lees, A.J., Rees, G., Weil, R.S., 2020a. Differences in network controllability and regional gene expression underlie hallucinations in Parkinson's disease. Brain 143, 3435–3448. doi:10.1093/brain/awaa270.

Zarkali, A., McColgan, P., Ryten, M., Reynolds, R.H., Leyland, L.A., Lees, A.J., Rees, G., Weil, R.S., 2020b. Dementia risk in Parkinson's disease is associated with inter-hemispheric connectivity loss and determined by regional gene expression. NeuroImage: Clinical 28, 102470. doi:10.1016/j.nicl.2020.102470.

Zeisel, A., Muñoz Manchado, A.B., Codeluppi, S., Lönnerberg, P., Manno, G.L., Juréus, A., Marques, S., Munguba, H., He, L., Betsholtz, C., Rolny, C., Castelo-Branco, G., Hjerling-Leffler, J., Linnarsson, S., 2015. Cell types in the mouse cortex and hippocampus revealed by single-cell RNA-seq. Science 347, 1138–1142. doi:10.1126/science.aaa1934.

Zhao, Y., Wen, J., Cross, A.H., Yablonskiy, D.A., 2016. On the relationship between cellular and hemodynamic properties of the human brain cortex throughout adult lifespan. NeuroImage 133, 417–429. doi:10.1016/j.neuroimage.2016.03.022.

Zurkiya, O., Hu, X., 2006. Off-resonance saturation as a means of generating contrast with superparamagnetic nanoparticles. Magnetic Resonance in Medicine 56, 726–732. doi:10.1002/mrm.21024.

Supplementary Material

Full EWCE results

Below are the complete results of the EWCE analyses. These results include cell types only present as a cell type in one of the cell type-specific datasets, which were for this reason omitted from the main manuscript as this meant a replication analysis could not performed (see Materials and Methods). They also include the results at the level of the top 10 and 20% of genes associated with each parameter in addition to those at the top 5% level (most of which were presented in Figures 3–5 in the main text).

Figures S1–S3 show the EWCE results with the SMART-seq dataset for the top 5, 10, and 20% of genes positively (upweighted) and negatively (downweighted) associated with each qMRI parameter in the first PLS component.

Figures S4–S6 show the EWCE results with the DroNc-seq dataset for the top 5, 10, and 20% of genes positively (upweighted) and negatively (downweighted) associated with each qMRI parameter in the first PLS component.

Figures S7–S9 show the EWCE results with the SMART-seq dataset for the top 5, 10, and 20% of genes positively (upweighted) and negatively (downweighted) associated with each qMRI parameter in the second PLS component.

Figures S10–S12 show the EWCE results with the DroNc-seq dataset for the top 5, 10, and 20% of genes positively (upweighted) and negatively (downweighted) associated with each qMRI parameter in the second PLS component.

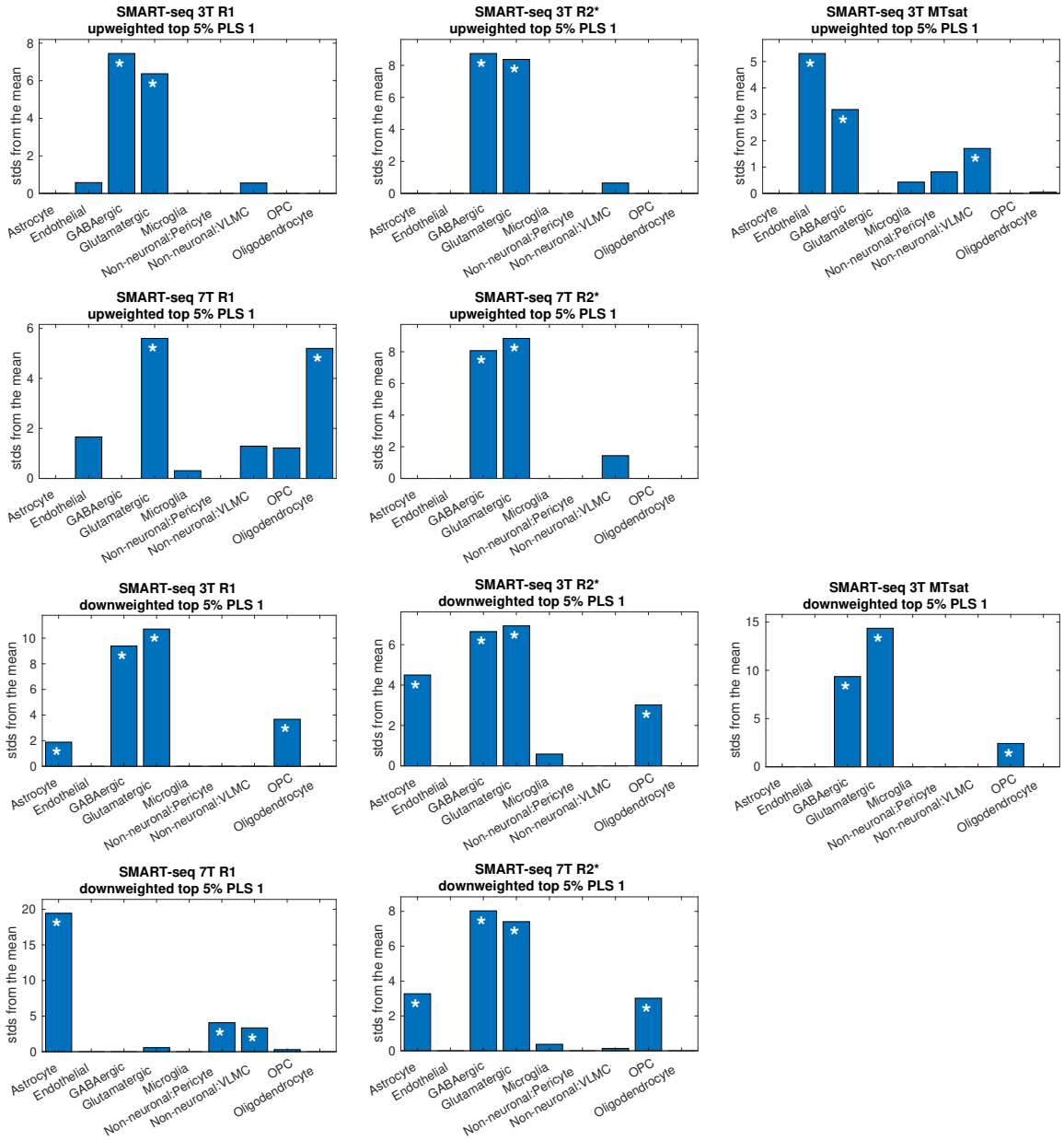

Figure S1: EWCE results on top 5% of up- and downweighted genes associated with PLS component 1 of each parameter using SMART-seq gene lists. MT: MTsat, VLMC: vascular and leptomeningeal cells, OPC: oligodendrocyte precursor cells. Bars are only plotted when FDR-corrected $p < 0.5$. *: FDR-corrected $p < 0.05$.

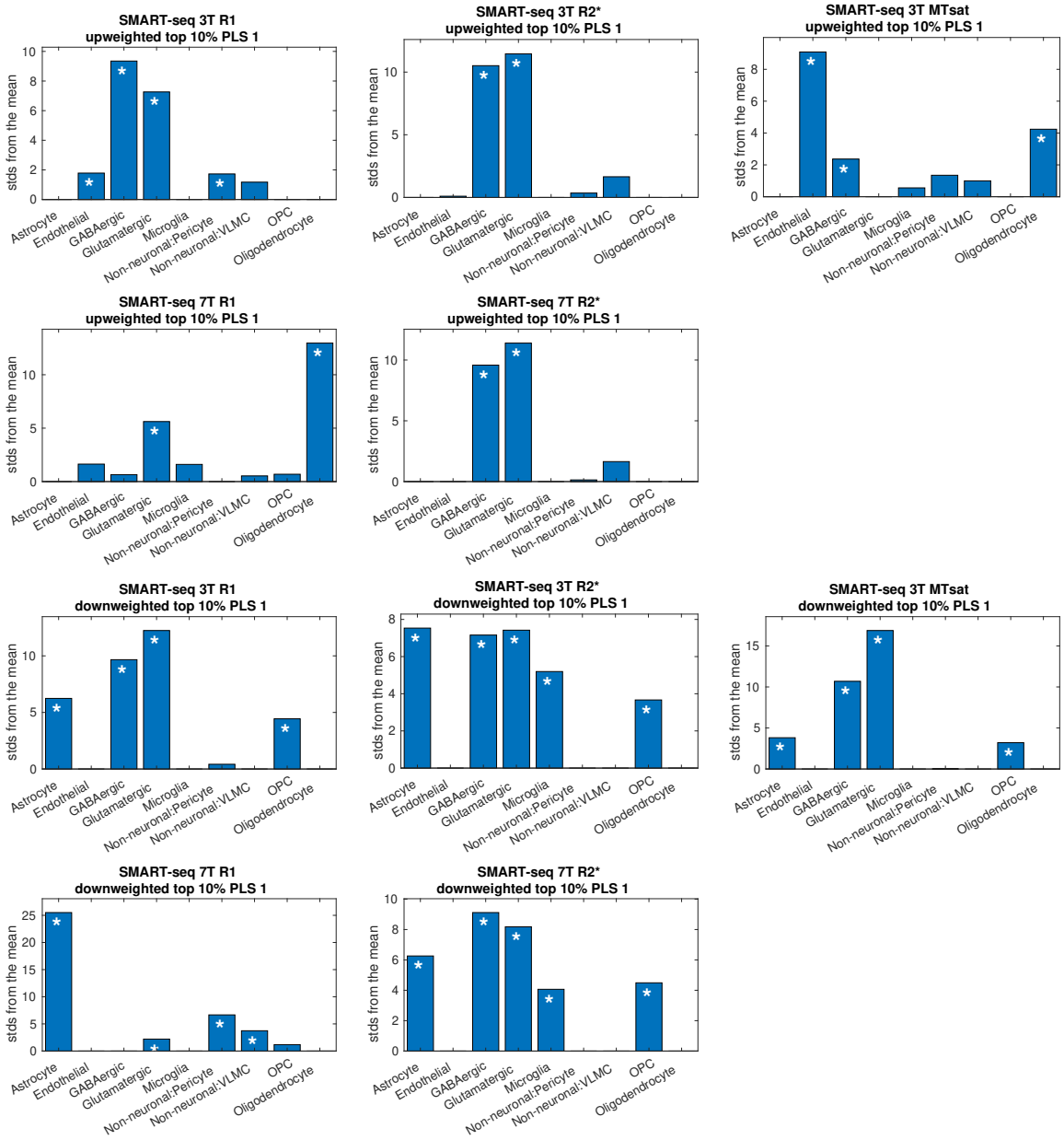

Figure S2: EWCE results on top 10% of up- and downweighted genes associated with PLS component 1 of each parameter using SMART-seq gene lists. MT: MTsat, VLMC: vascular and leptomeningeal cells, OPC: oligodendrocyte precursor cells. Bars are only plotted when FDR-corrected $p < 0.5$. *: FDR-corrected $p < 0.05$.

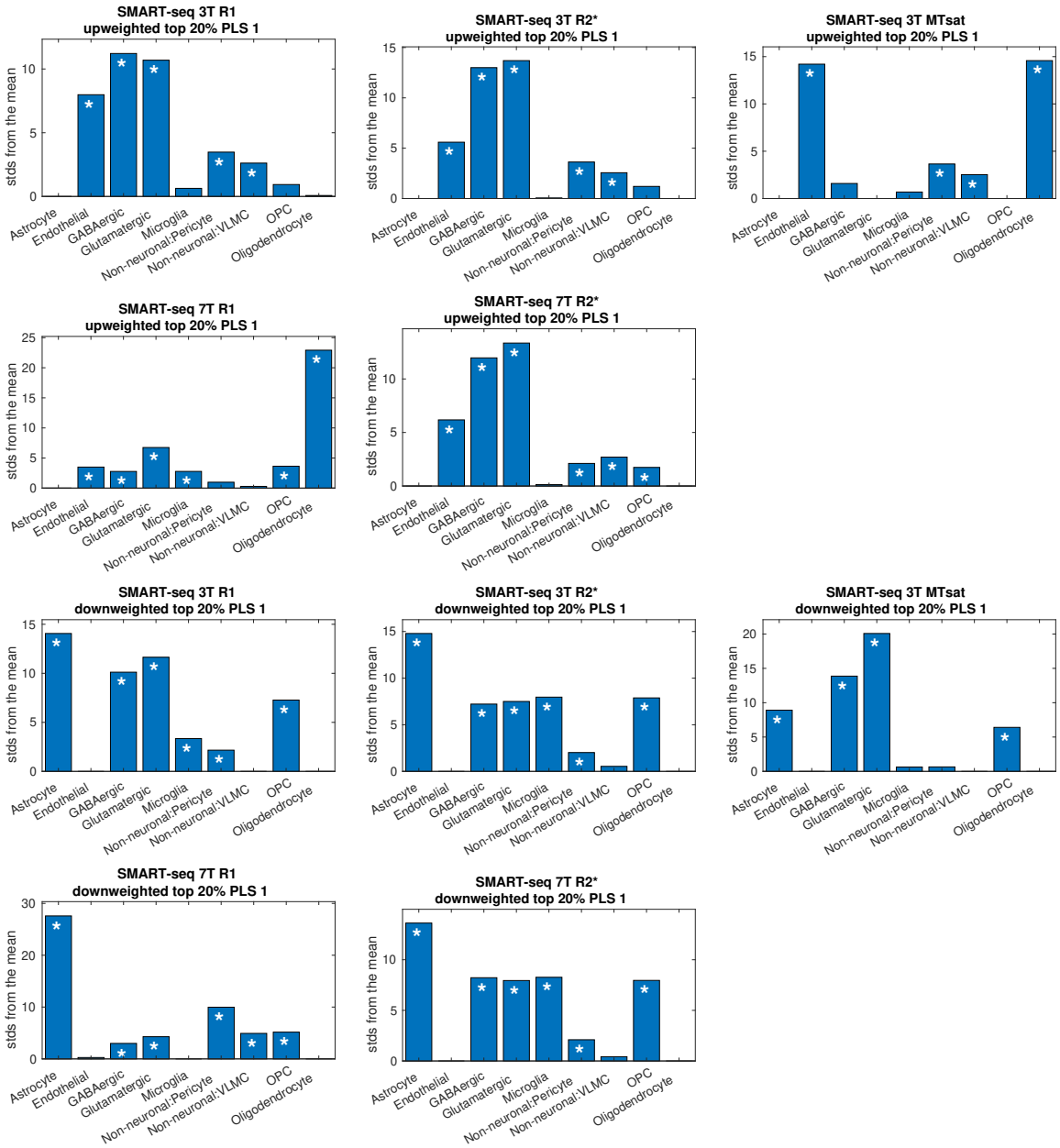

Figure S3: EWCE results on top 20% of up- and downweighted genes associated with PLS component 1 of each parameter using SMART-seq gene lists. MT: MTsat, VLMC: vascular and leptomeningeal cells, OPC: oligodendrocyte precursor cells. Bars are only plotted when FDR-corrected $p < 0.5$. *: FDR-corrected $p < 0.05$.

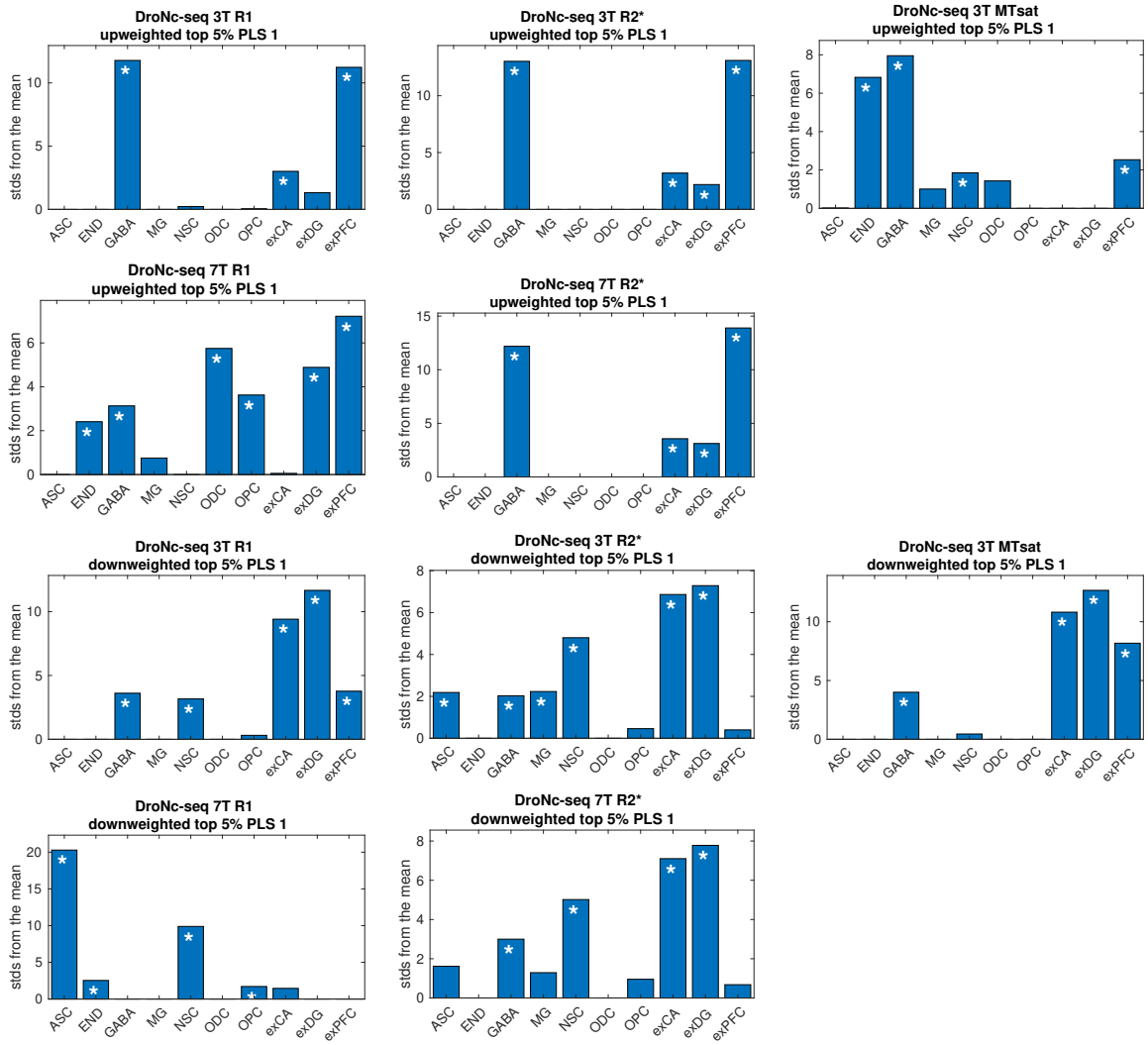

Figure S4: EWCE results on top 5% of up- and downweighted genes associated with PLS component 1 of each parameter using DroNc-seq gene lists. MT: MTsat, ASC: astrocytes, END: endothelial cells, exCA: pyramidal neurons from the hippocampal CA region, exDG: granule neurons from the hippocampal dentate gyrus region, exPFC: glutamatergic neurons from the prefrontal cortex, GABA: GABAergic (inhibitory) neurons, MG: microglia, NSC: neuronal stem cells, ODC: oligodendrocytes, OPC: oligodendrocyte precursor cells. Bars are only plotted when FDR-corrected $p < 0.5$. *: FDR-corrected $p < 0.05$.

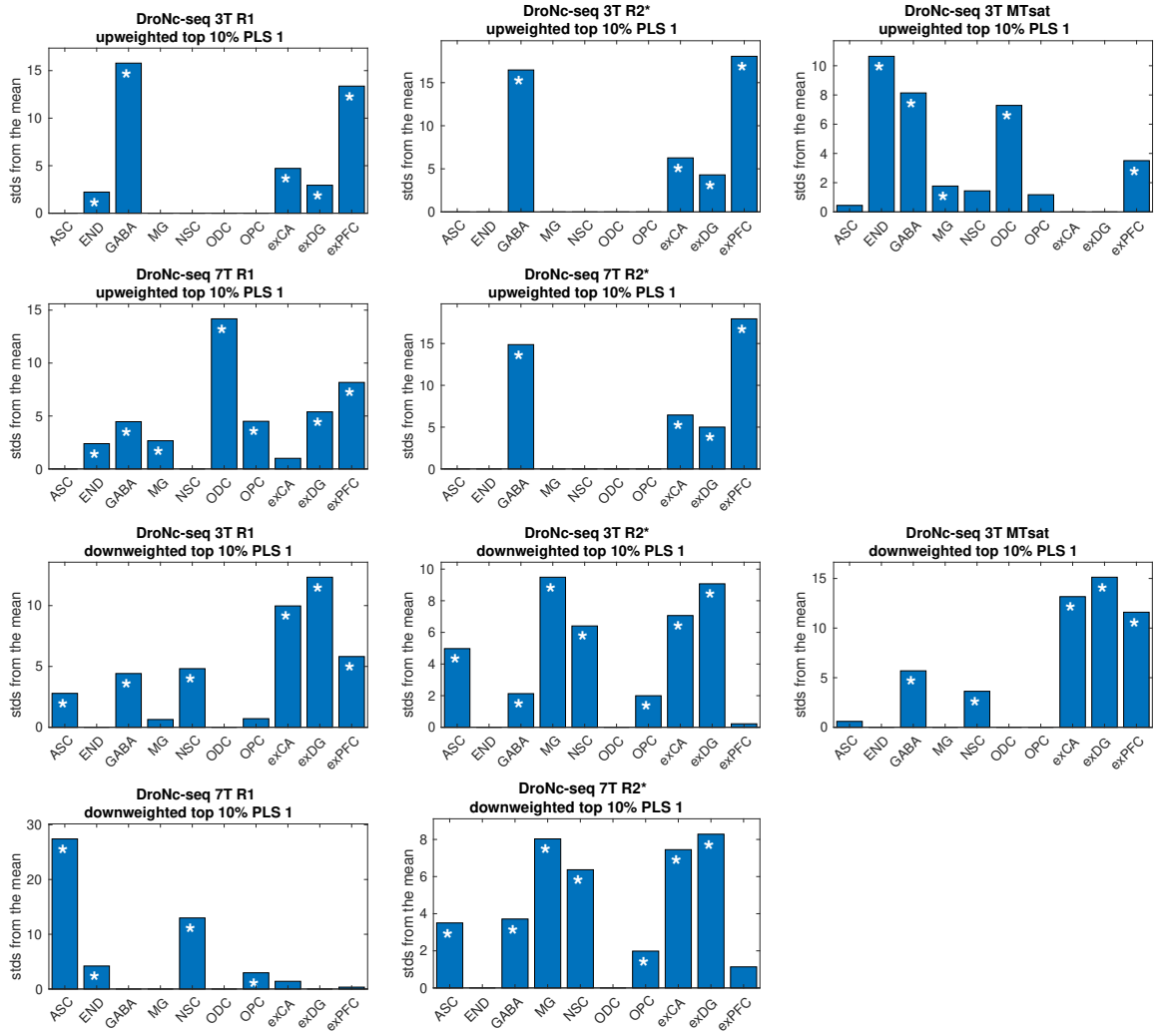

Figure S5: EWCE results on top 10% of up- and downweighted genes associated with PLS component 1 of each parameter using DroNc-seq gene lists. MT: MTsat, ASC: astrocytes, END: endothelial cells, exCA: pyramidal neurons from the hippocampal CA region, exDG: granule neurons from the hippocampal dentate gyrus region, exPFC: glutamatergic neurons from the prefrontal cortex, GABA: GABAergic (inhibitory) neurons, MG: microglia, NSC: neuronal stem cells, ODC: oligodendrocytes, OPC: oligodendrocyte precursor cells. Bars are only plotted when FDR-corrected $p < 0.5$. *: FDR-corrected $p < 0.05$.

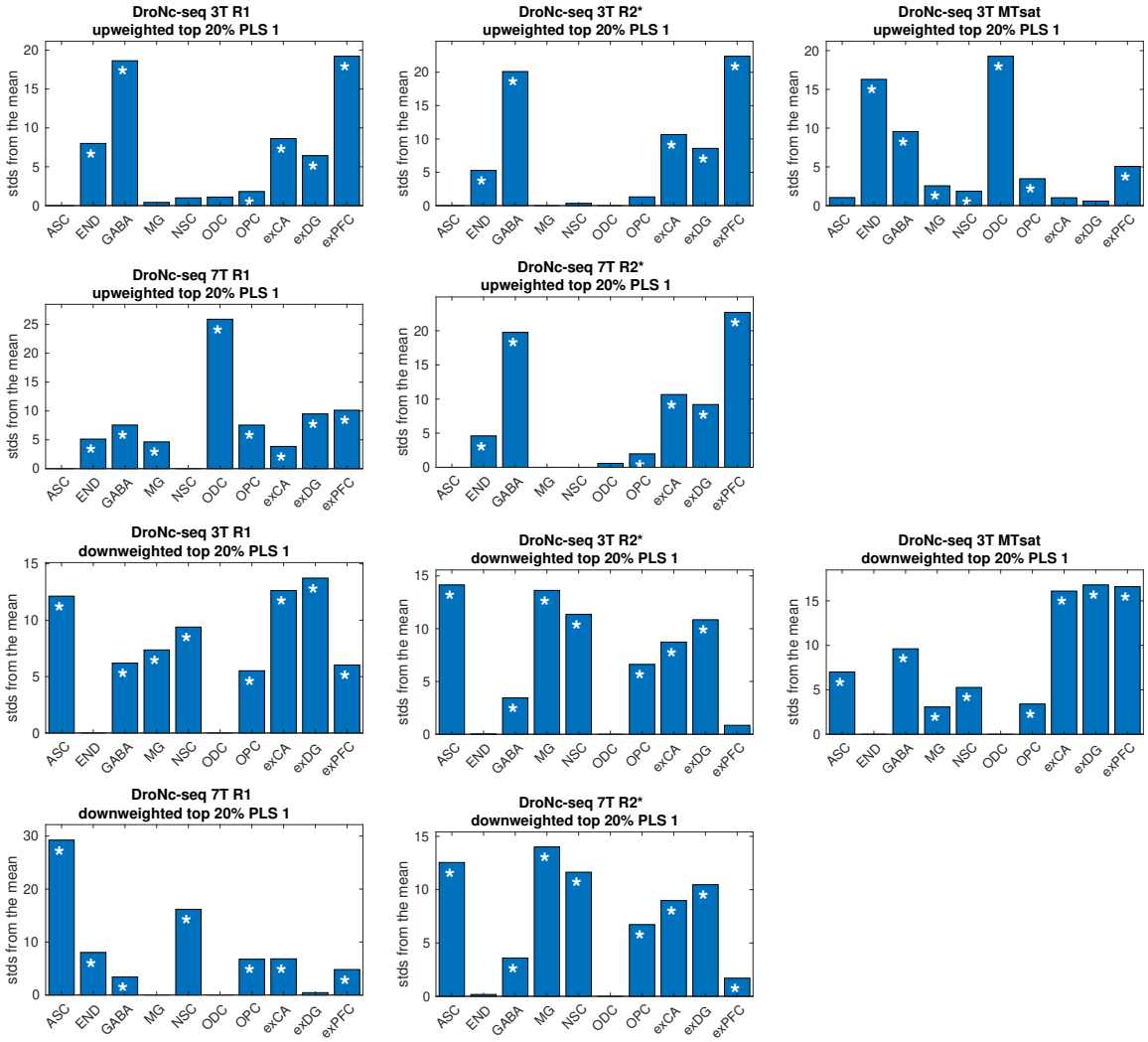

Figure S6: EWCE results on top 20% of up- and downweighted genes associated with PLS component 1 of each parameter using DroNc-seq gene lists. MT: MTsat, ASC: astrocytes, END: endothelial cells, exCA: pyramidal neurons from the hippocampal CA region, exDG: granule neurons from the hippocampal dentate gyrus region, exPFC: glutamatergic neurons from the prefrontal cortex, GABA: GABAergic (inhibitory) neurons, MG: microglia, NSC: neuronal stem cells, ODC: oligodendrocytes, OPC: oligodendrocyte precursor cells. Bars are only plotted when FDR-corrected $p < 0.5$. *: FDR-corrected $p < 0.05$.

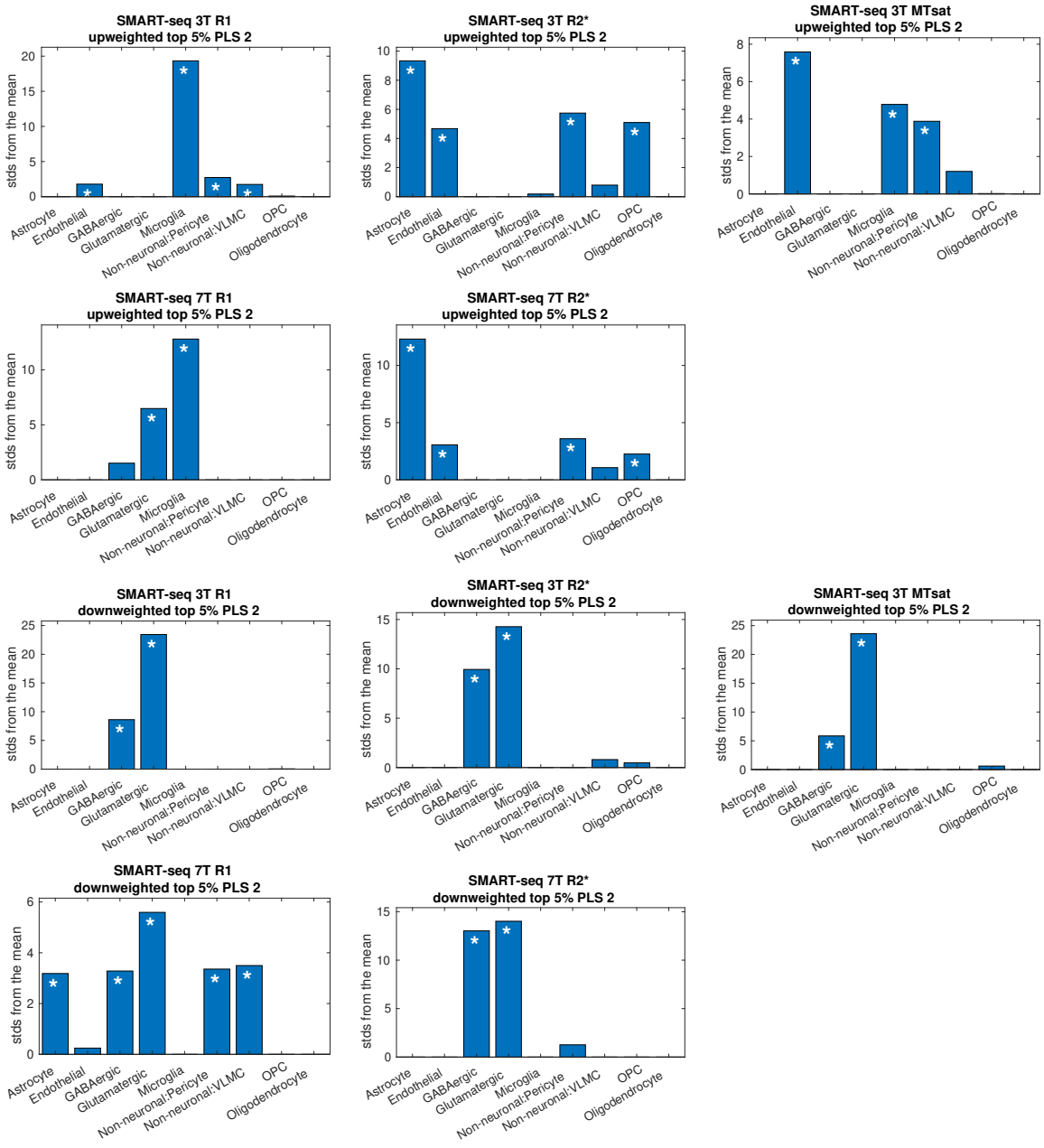

Figure S7: EWCE results on top 5% of up- and downweighted genes associated with PLS component 2 of each parameter using SMART-seq gene lists. MT: MTsat, VLMC: vascular and leptomeningeal cells, OPC: oligodendrocyte precursor cells. Bars are only plotted when FDR-corrected $p < 0.5$. *: FDR-corrected $p < 0.05$.

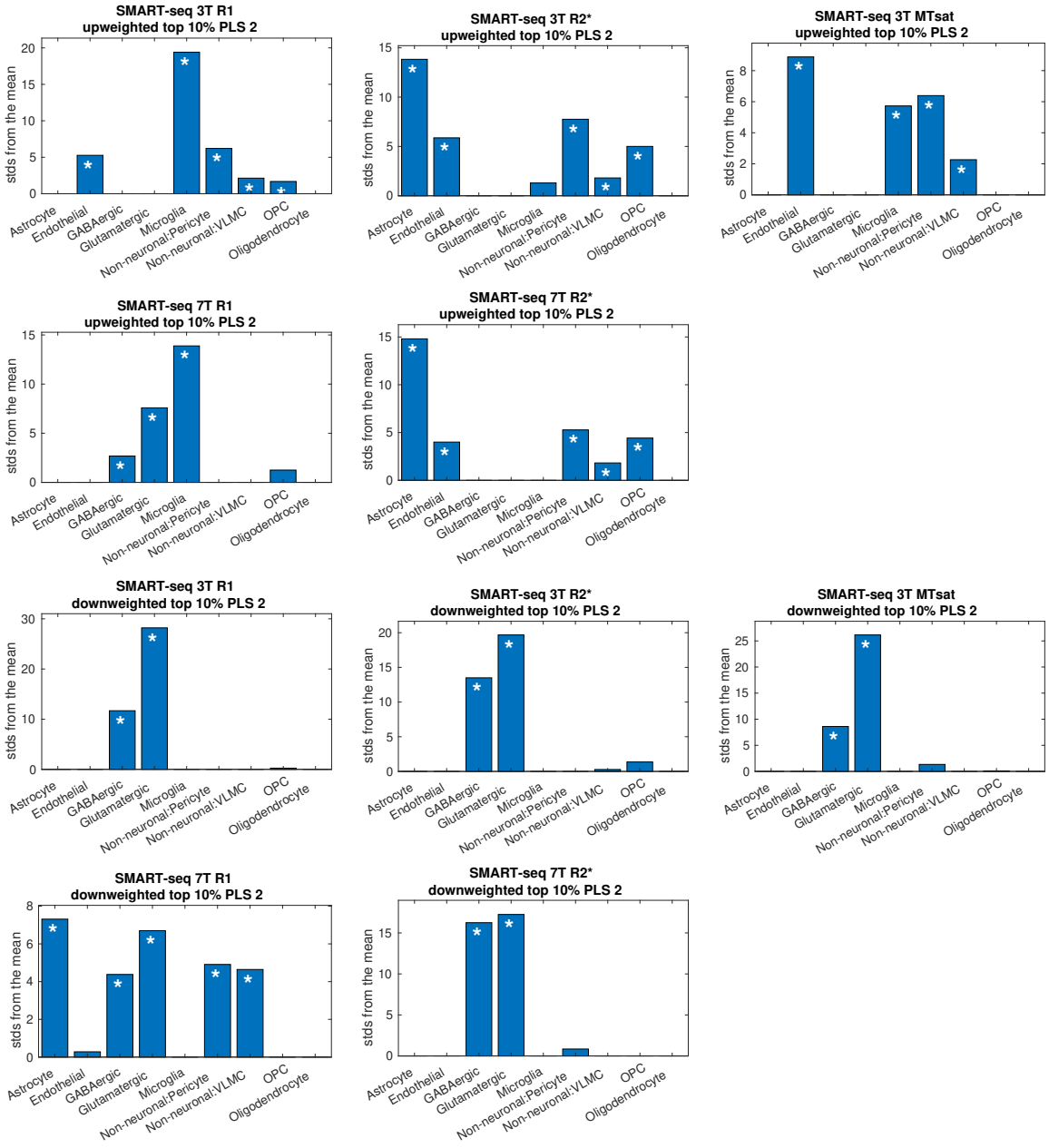

Figure S8: EWCE results on top 10% of up- and downweighted genes associated with PLS component 2 of each parameter using SMART-seq gene lists. MT: MTsat, VLMC: vascular and leptomeningeal cells, OPC: oligodendrocyte precursor cells. Bars are only plotted when FDR-corrected $p < 0.5$. *: FDR-corrected $p < 0.05$.

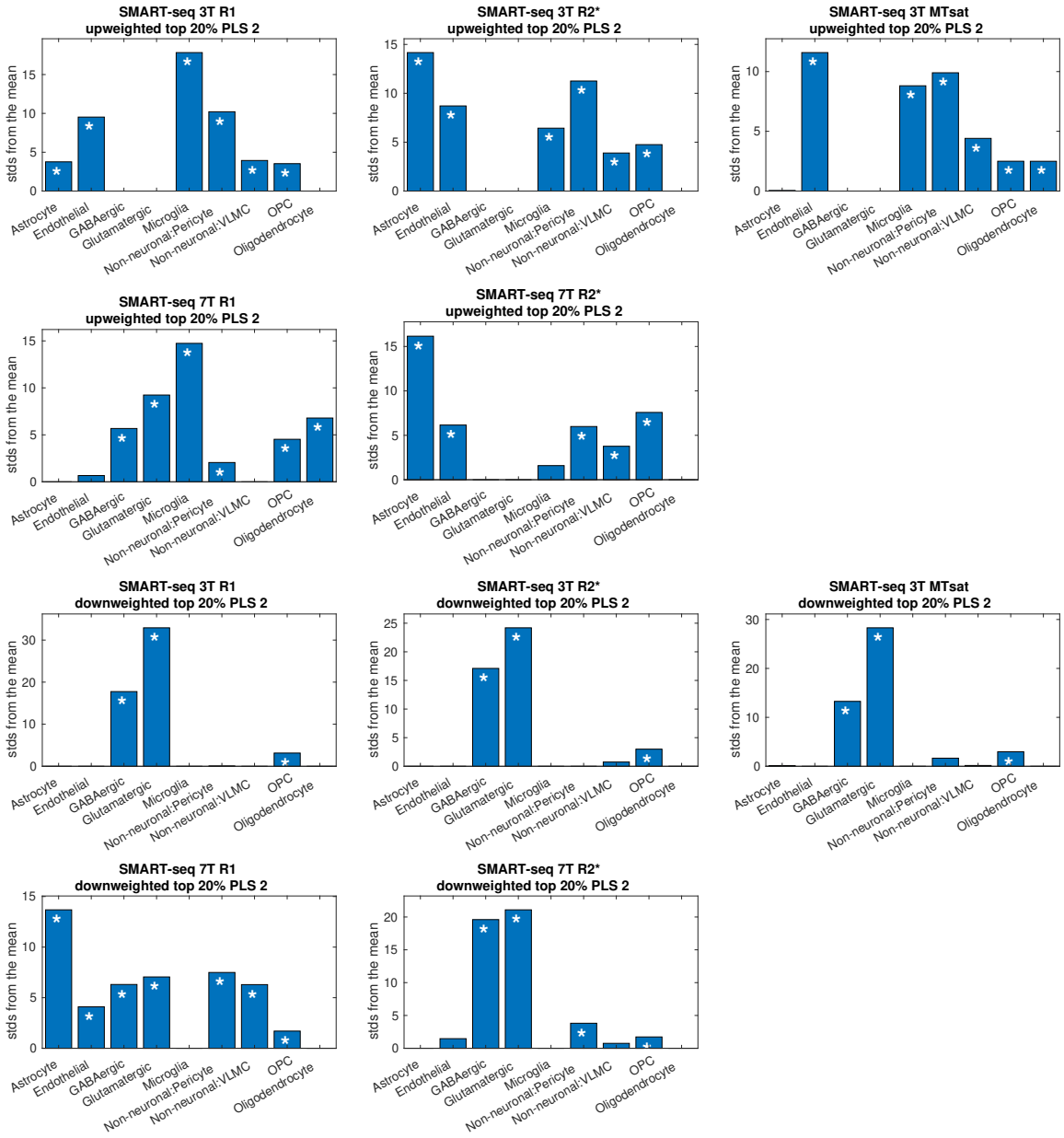

Figure S9: EWCE results on top 20% of up- and downweighted genes associated with PLS component 2 of each parameter using SMART-seq gene lists. MT: MTsat, VLMC: vascular and leptomeningeal cells, OPC: oligodendrocyte precursor cells. Bars are only plotted when FDR-corrected $p < 0.5$. *: FDR-corrected $p < 0.05$.

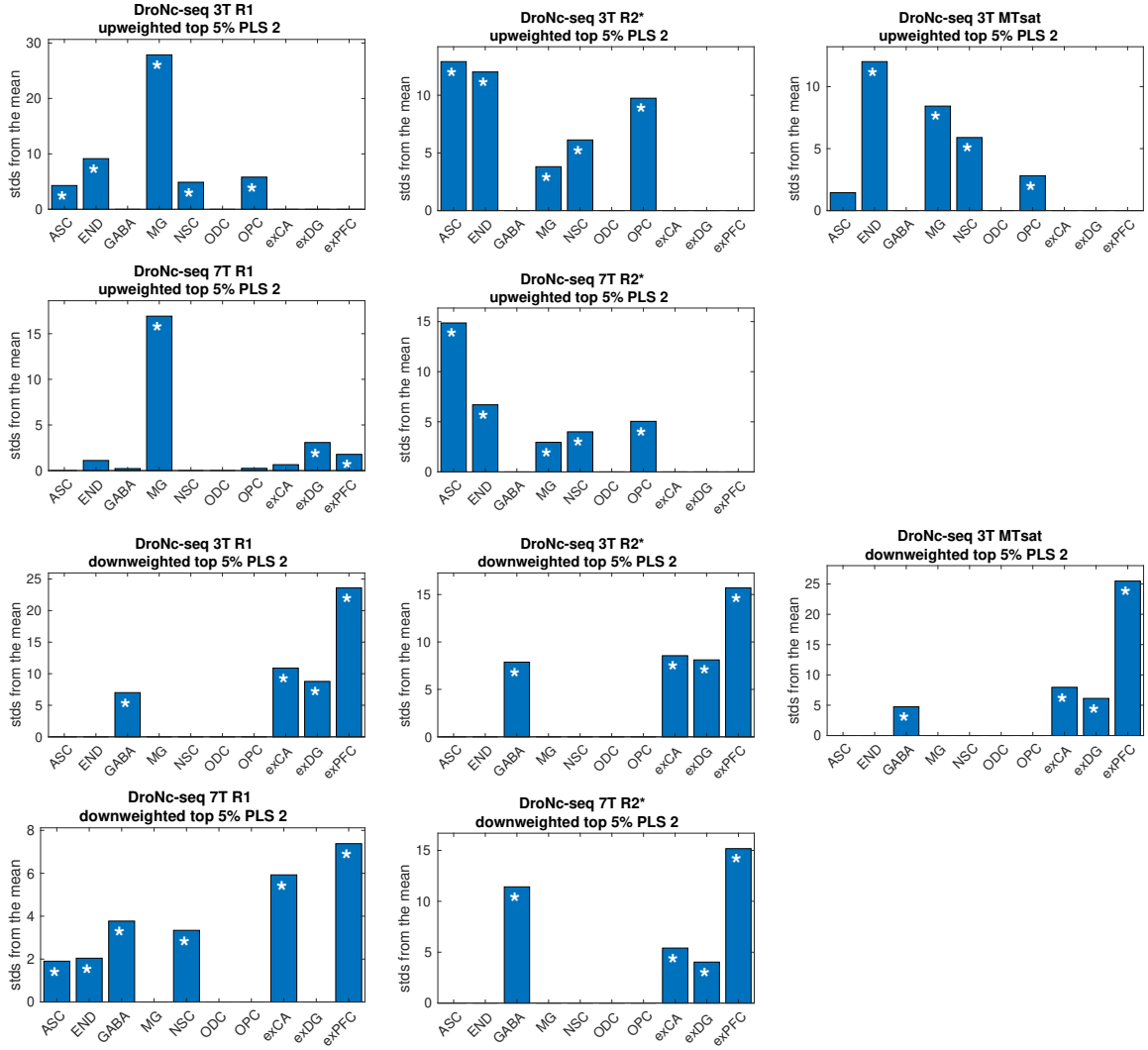

Figure S10: EWCE results on top 5% of up- and downweighted genes associated with PLS component 2 of each parameter using DroNc-seq gene lists. MT: MTsat, ASC: astrocytes, END: endothelial cells, exCA: pyramidal neurons from the hippocampal CA region, exDG: granule neurons from the hippocampal dentate gyrus region, exPFC: glutamatergic neurons from the prefrontal cortex, GABA: GABAergic (inhibitory) neurons, MG: microglia, NSC: neuronal stem cells, ODC: oligodendrocytes, OPC: oligodendrocyte precursor cells. Bars are only plotted when FDR-corrected $p < 0.5$. *: FDR-corrected $p < 0.05$.

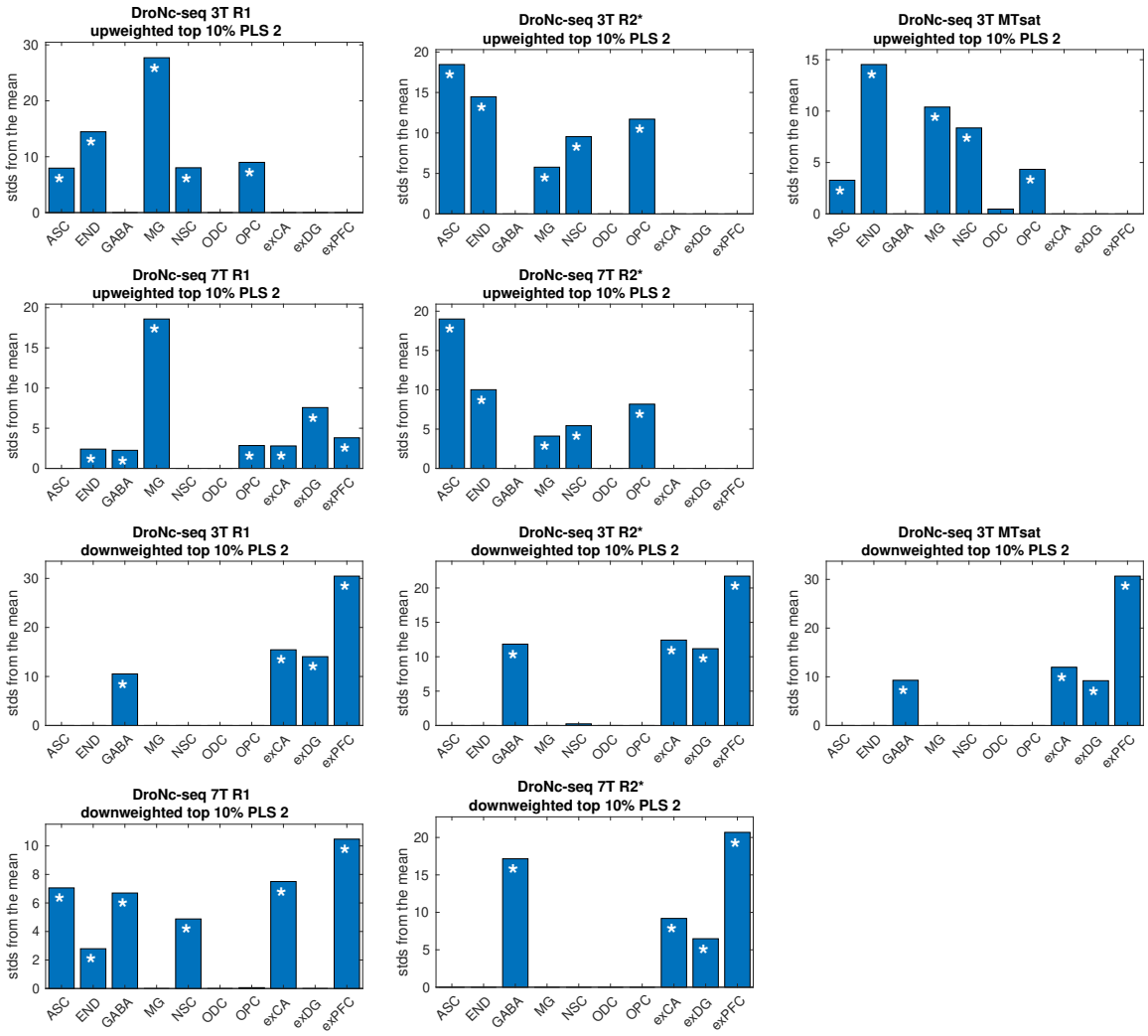

Figure S11: EWCE results on top 10% of up- and downweighted genes associated with PLS component 2 of each parameter using DroNc-seq gene lists. MT: MTsat, ASC: astrocytes, END: endothelial cells, exCA: pyramidal neurons from the hippocampal CA region, exDG: granule neurons from the hippocampal dentate gyrus region, exPFC: glutamatergic neurons from the prefrontal cortex, GABA: GABAergic (inhibitory) neurons, MG: microglia, NSC: neuronal stem cells, ODC: oligodendrocytes, OPC: oligodendrocyte precursor cells. Bars are only plotted when FDR-corrected $p < 0.5$. *: FDR-corrected $p < 0.05$.

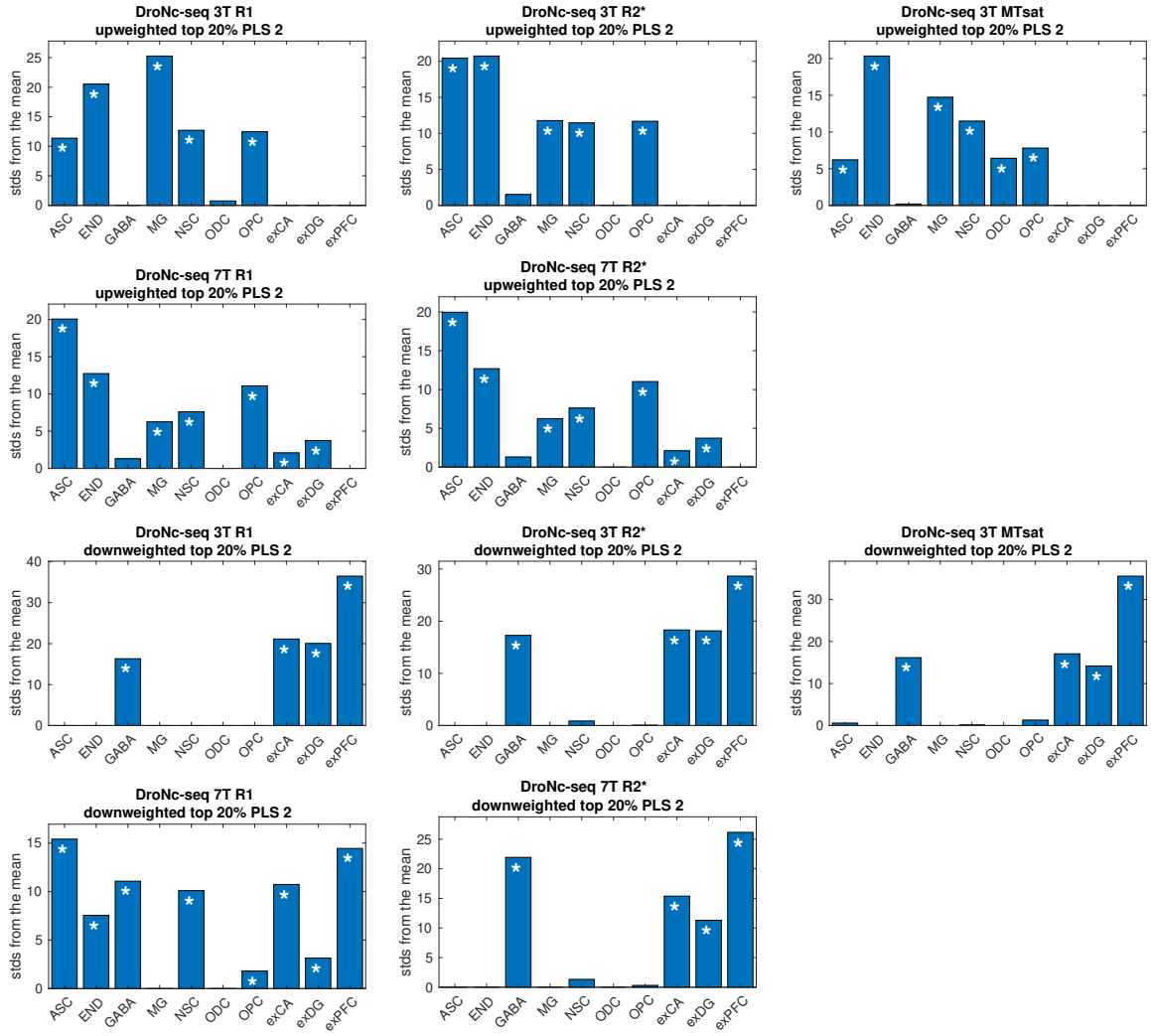

Figure S12: EWCE results on top 20% of up- and downweighted genes associated with PLS component 2 of each parameter using DroNc-seq gene lists. MT: MTsat, ASC: astrocytes, END: endothelial cells, exCA: pyramidal neurons from the hippocampal CA region, exDG: granule neurons from the hippocampal dentate gyrus region, exPFC: glutamatergic neurons from the prefrontal cortex, GABA: GABAergic (inhibitory) neurons, MG: microglia, NSC: neuronal stem cells, ODC: oligodendrocytes, OPC: oligodendrocyte precursor cells. Bars are only plotted when FDR-corrected $p < 0.5$. *: FDR-corrected $p < 0.05$.

R_1 7T results excluding potentially artefact-affected areas

Below are the results of the EWCE analyses for both the SMART-seq and DroNc-seq cell type-specific datasets with gene lists comprising the top 5, 10, and 20% of genes positively (upweighted) and negatively (downweighted) associated with R_1 at 7T in each PLS component after removal of areas potentially strongly affected by B_1 and B_0 artefacts (see Materials and Methods). Table S1 shows the variance explained in the PLS components after removal of these areas, Figure S13 shows the results for the top 5% of genes associated with R_1 at 7T (cf. Figure 5), and Figures S14 and S15 show the full EWCE results for the first and second PLS component, respectively (cf. Figures S1–S12).

	PLS component	Spatial variance explained in: gene distribution	qMRI parameter
R_1 7T	1	17%	18%
	2	9%	20%

Table S1: Variance explained by the PLS components for R_1 at 7T after removal of areas potentially strongly affected by B_1 and B_0 artefacts (cf. Table 1 in the main manuscript).

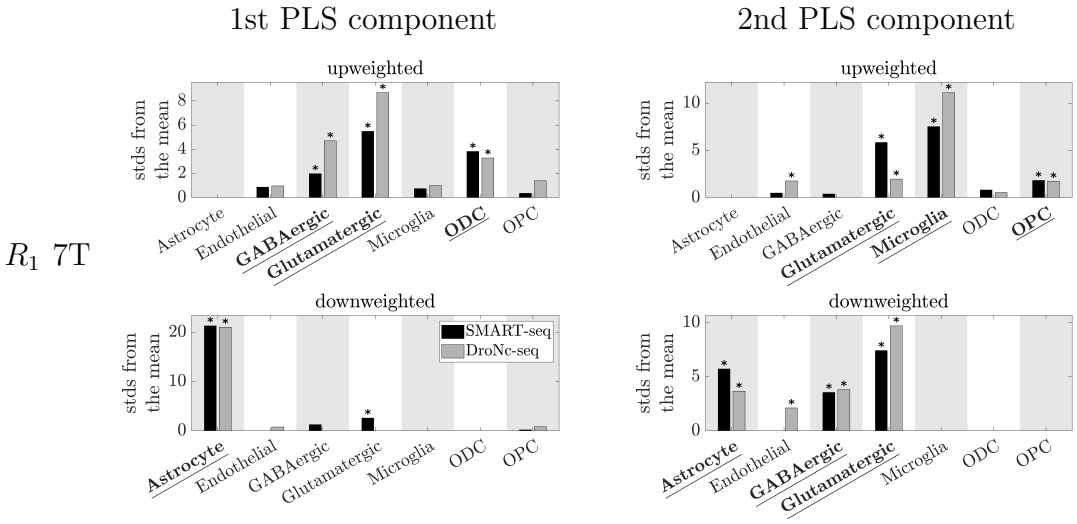

Figure S13: EWCE results showing the cell type associations of the top 5% of genes associated with R_1 at 7T after excluding inferior regions associated with B_1 and B_0 artefacts (cf. Figure 5 in the main manuscript). Plotted are the number of standard deviations (stds) by which the EWCE value deviated from the mean value over bootstrapped target lists. Results from the two cell type-specific datasets are plotted in different colours: SMART-seq in black, DroNc-seq in grey. Left: First component of the PLS. Right: Second component of the PLS. Bars are only plotted when FDR-corrected $p < 0.5$. *: FDR-corrected $p < 0.05$. Significant cell type associations which replicated between both cell type-specific datasets (robust results) are underlined and in bold.

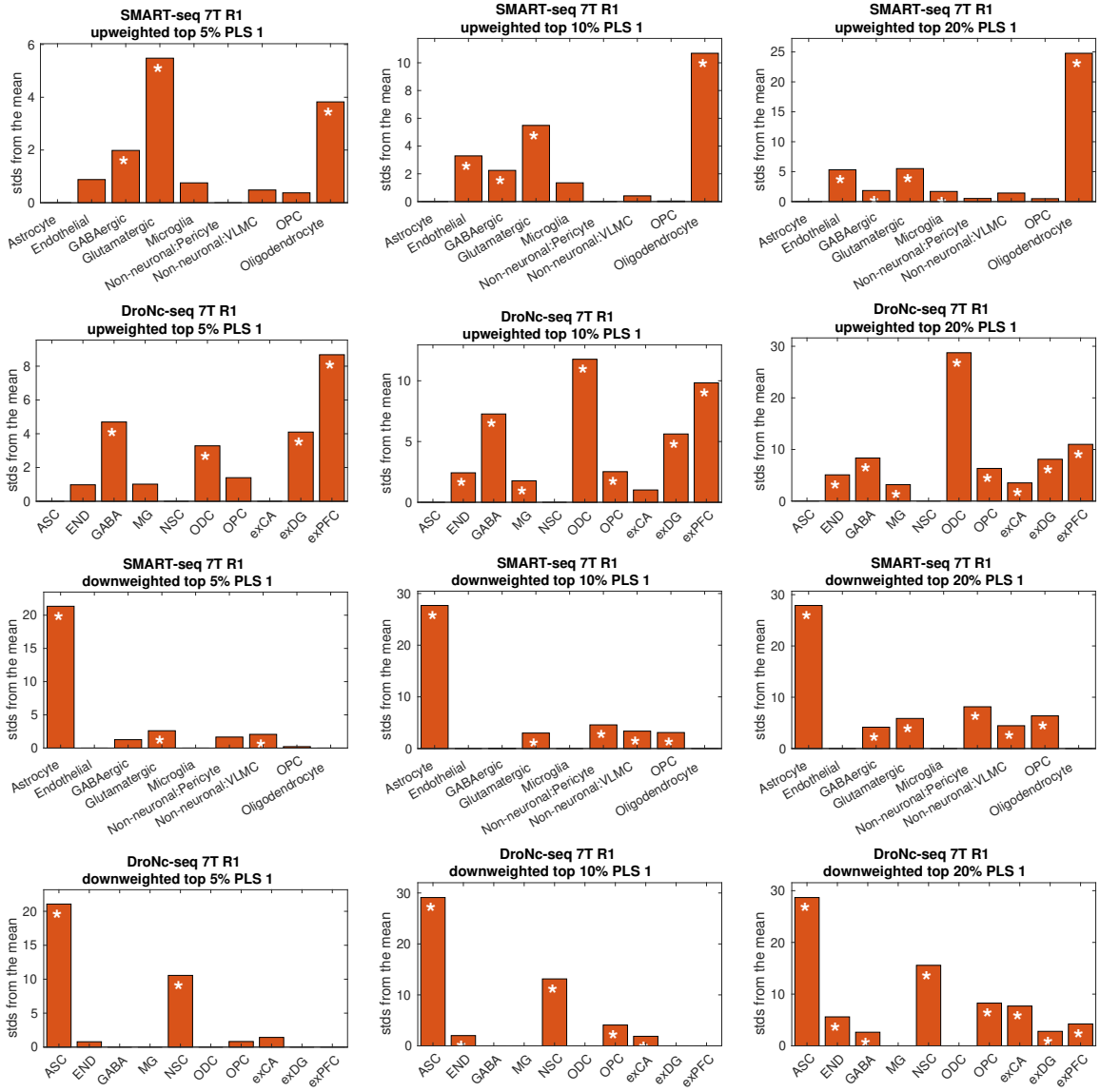

Figure S14: EWCE results on top 5, 10 and 20% of up- and downweighted genes associated with PLS component 1 of R_1 in both cell type-specific gene lists after excluding inferior regions associated with B_1 and B_0 artefacts. ASC: astrocytes, END: endothelial cells, exCA: pyramidal neurons from the hippocampal CA region, exDG: granule neurons from the hippocampal dentate gyrus region, exPFC: glutamatergic neurons from the prefrontal cortex, GABA: GABAergic (inhibitory) neurons, MG: microglia, NSC: neuronal stem cells, ODC: oligodendrocytes, OPC: oligodendrocyte precursor cells, VLMC: vascular and leptomeningeal cells. Bars are only plotted when FDR-corrected $p < 0.5$. *: FDR-corrected $p < 0.05$.

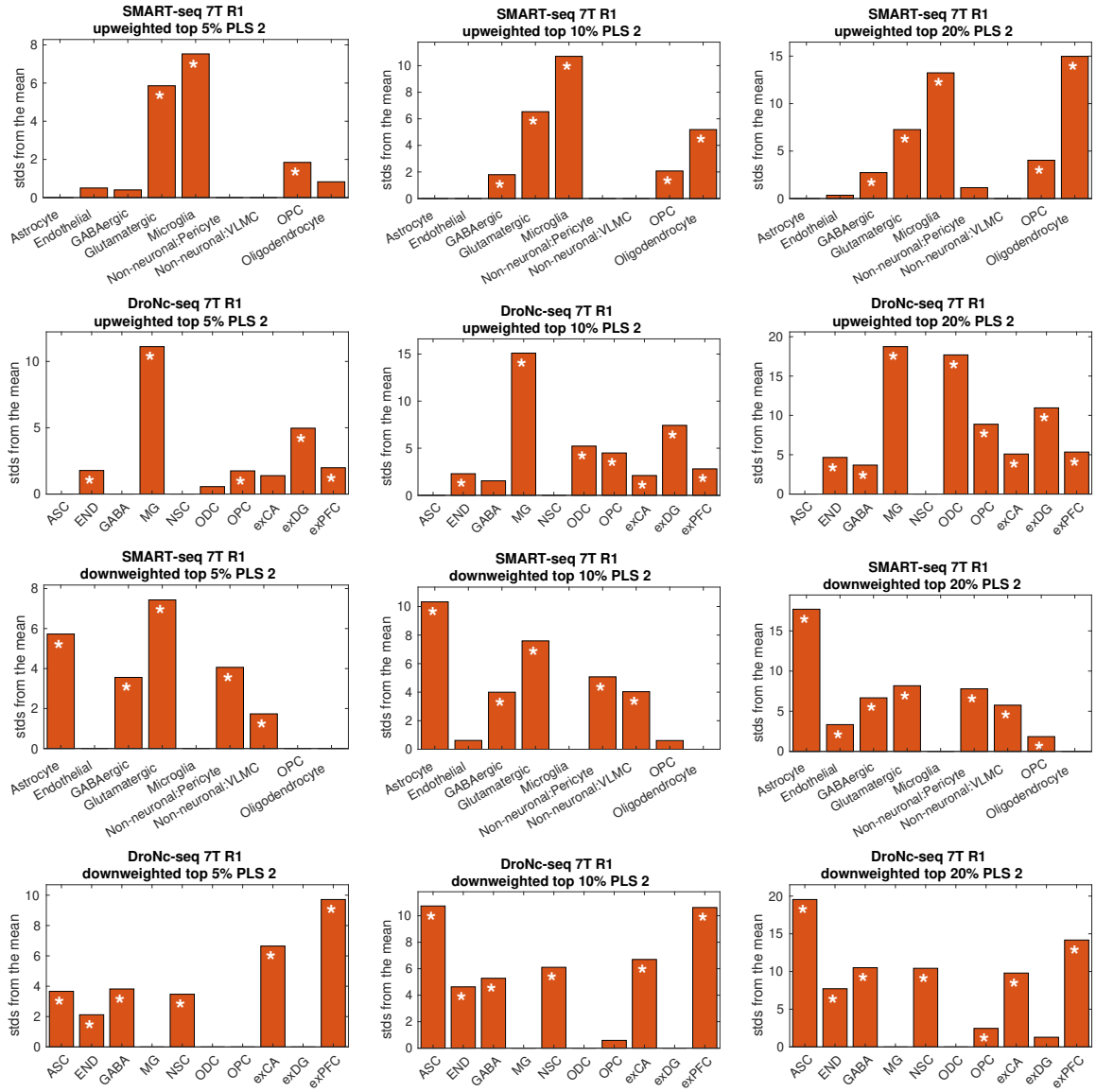

Figure S15: EWCE results on top 5, 10 and 20% of up- and downweighted genes associated with PLS component 2 of R_1 in both cell type-specific gene lists after excluding inferior regions associated with B_1 and B_0 artefacts. ASC: astrocytes, END: endothelial cells, exCA: pyramidal neurons from the hippocampal CA region, exDG: granule neurons from the hippocampal dentate gyrus region, exPFC: glutamatergic neurons from the prefrontal cortex, GABA: GABAergic (inhibitory) neurons, MG: microglia, NSC: neuronal stem cells, ODC: oligodendrocytes, OPC: oligodendrocyte precursor cells, VLMC: vascular and leptomeningeal cells. Bars are only plotted when FDR-corrected $p < 0.5$. *: FDR-corrected $p < 0.05$.